Reaction mechanism and kinetics of CO oxidation over a CuO/Ce$_{0.75}$Zr$_{0.25}$O$_2$-δ catalyst

Running Kang[a,b], Xiaolin Wei[a,b], Feng Bin[a,*], Zibing Wang[c], Qinglan Hao[d], Baojuan Dou[d,*]

[a] State Key Laboratory of High-Temperature Gas Dynamics, Institute of Mechanics, Chinese Academy of Sciences, 100190 Beijing, PR China
[b] School of Engineering Science, University of Chinese Academy of Sciences, 100049 Beijing, PR China
[c] College of Metallurgy and Energy, North China University of Science and Technology, 063210 Tangshan, PR China
[d] College of Environmental Sciences, Tianjin University of Science & Technology, Tianjin 300457, PR China

ARTICLE INFO

ABSTRACT

The CuO/Ce$_{0.75}$Zr$_{0.25}$O$_2$-δ and Ce$_{0.75}$Zr$_{0.25}$O$_δ$ catalysts were prepared by the sol-gel method, and Cu$_{0.07}$Ce$_{0.75}$Zr$_{0.25}$O$_2$-δ was obtained by treating CuO/Ce$_{0.75}$Zr$_{0.25}$O$_2$-δ with nitric acid to remove the well-dispersed CuO on the surface. Various characterizations were used to reveal the different active sites, such as surface-dispersed CuO and Cu-Ce-Zr-O$_δ$ solid solutions in CuO/Ce$_{0.75}$Zr$_{0.25}$O$_2$-δ, Cu-Ce-Zr-O$_δ$ solid solutions in Cu$_{0.07}$Ce$_{0.75}$Zr$_{0.25}$O$_2$-δ and Ce-Zr-O$_δ$ solid solutions in Ce$_{0.75}$Zr$_{0.25}$O$_δ$. The Raman and O$_2$-TPD results showed that the concentration of oxygen vacancies in Cu-Ce-Zr-O$_δ$ solid solutions was higher than that in Ce-Zr-O$_δ$ solid solutions. CO oxidation testing suggested that the catalytic activity decreases in the order of CuO/Ce$_{0.75}$Zr$_{0.25}$O$_2$-δ > Cu$_{0.07}$Ce$_{0.75}$Zr$_{0.25}$O$_2$-δ > Ce$_{0.75}$Zr$_{0.25}$O$_δ$. Combined with the in situ diffuse-reflectance Fourier transform (in situ DRIFT) results, the reaction sensitivity followed the order of CO linear chemisorption onto dispersed CuO$_x$ species (Mars-van Krevelen mechanism) > carbonate species onto a Cu-Ce-Zr-O$_δ$ solid solution (Langmuir-Hinshelwood mechanism) > carbonate species onto a Ce-Zr-O$_δ$ solid solution (Langmuir-Hinshelwood mechanism). Kinetic studies suggested that the power-law rate expressions and apparent activation energies were r = 6.02 × 10^{-7} × P$_{CO}$$^{0.68}P_{O2}$$^{0.03}$ (53 ± 3 kJ/mol) for CuO/Ce$_{0.75}$Zr$_{0.25}$O$_2$-δ, r = 5.86 × 10^{-7} × P$_{CO}$$^{0.8}P_{O2}$$^{0.07}$ (105 ± 5 kJ/mol) for Cu$_{0.07}$Ce$_{0.75}$Zr$_{0.25}$O$_2$-δ and r = 5.7 × 10^{-7} × P$_{CO}$$^{0.75}P_{O2}$$^{0.12}$ (115 ± 6 kJ/mol) for Ce$_{0.75}$Zr$_{0.25}$O$_δ$. The Mars-van Krevelen mechanism should be the crucial reaction pathway over CuO/Ce$_{0.75}$Zr$_{0.25}$O$_2$-δ in CO interfacial reactions, although the Langmuir-Hinshelwood mechanism cannot be ignored, and the Langmuir-Hinshelwood mechanism mainly occurred over the Cu$_{0.07}$Ce$_{0.75}$Zr$_{0.25}$O$_2$-δ and Ce$_{0.75}$Zr$_{0.25}$O$_δ$ catalysts, where the contribution from the Mars-van Krevelen mechanism was negligible due to the absence of surface CuO$_x$ species.

1. Introduction

The catalytic oxidation of carbon monoxide (CO) is an important topic because of its numerous practical applications, including low-temperature CO oxidation, preferential CO oxidation and automotive exhaust control [1–3]. Among the various proposed heterogeneous catalysts, mixed metal oxide catalysts containing Cu, Ce and Zr have attracted great interest in low-temperature CO oxidation because of their low cost and good sintering resistance, which are comparable or superior to those of noble metal catalysts [4,5]. In these mixed metal oxide catalysts, Cu species are active and show superior CO chemisorption via the Cu^{2+}-Cu$^+$ couple. CeO$_2$ not only promotes dispersion of the active Cu species but also provides a large oxygen storage capacity because of the Ce^{4+}-Ce^{3+} redox couple in cubic fluorite

structures [6]. Although ZrO$_2$ cannot contribute to the catalytic activity directly, Zr that diffuses into the CeO$_2$ lattice strongly affects its thermal stability and may improve the catalyst performance through the formation of a Ce-Zr solid solution [7].

In recent years, many reports have focused on the structure-activity relationships and reaction mechanisms of CO oxidation over Cu-Ce-Zr catalysts [8–10]. With respect to structure-activity relationships, Qi et al. [11] found that Cu$^+$ species provided surface sites for CO chemisorption and that a high content of Ce^{3+} provided a better oxygen source, CeO$_2$, through the Cu^{2+} + Ce^{3+} ⇌ Cu$^+$ + Ce^{4+} redox equilibrium on the CuO-CeO$_2$ interface. The incorporation of Zr^{4+} reduced the formation energy of oxygen vacancies in Ce$_x$Zr$_{1-x}$O$_2$ (0.5 < × < 0.8) solid solutions, thus enhancing the reducibility and oxygen mobility of CeO$_2$ [7,12]. Liu et al. [10] confirmed that the

formation of a $Ce_{0.8}Zr_{0.2}O_2$ solid solution improved the dispersion of the CuO (active site) species, but they did not observe a Cu-Ce or Cu-Ce-Zr solid solution in the $CuO/Ce_{0.8}Zr_{0.2}O_2$ system. In further investigations, Luo et al. [13] studied the roles of different CuO species and found that finely dispersed CuO species on the catalyst surface exhibited the highest activity, whereas the Cu-Ce solid solution formed by substitution of Cu^{2+} in the CeO_2 lattice exhibited lower activity than $CuO-CeO_2$ catalysts. Despite intensive research concerning structure-activity relationships of Cu-Ce-Zr catalysts for CO oxidation, these relationships among CuO species, including the roles of dispersion, solid solution type, and the concentration of oxygen vacancies, still require further understanding. Knowledge of these relationships aids understanding of the reaction process and any synergistic effects, which is beneficial for the further design of Cu-Ce-Zr catalysts for CO oxidation [14].

The reaction mechanisms for CO oxidation over Cu-Ce-Zr catalysts, including details such as active sites and reaction pathways, remain a topic of debate. Sedmak et al. favored a Mars-van Krevelen (M-K) kinetic model based on the lattice oxygen involved in CO oxidation [15,16]. A more in-depth M-K mechanism was considered by Jia et al. [17], and its kinetic rate expression indicates that the surface CuO particles provide sites for CO chemisorption and that the lattice oxygen of the $Ce_{1-x}Cu_xO_{2-\sigma}$ solid solution can be active in CO oxidation over $CuO-CeO_2$ catalysts. Our previous investigation confirmed the pathways of CO chemisorption onto Cu^+/Cu^{2+} sites and the reaction of CO with lattice oxygen via the M-K mechanism for CO oxidation over CuCe/ZSM-5 catalysts [18]. However, Liu and Flytzani-Stephanopoulos [19] interpreted the CO oxidation behavior using a different rate expression that includes CO and O_2 adsorbing onto $CuO-CeO_2$ catalysts via the Langmuir-Hinshelwood (L-H) mechanism. Lee et al. [20] conducted a kinetics study and reported a detailed reaction pathway of the L-H mechanism, where CO absorbs onto the surface of CuO and reacts at Cu-Ce-O interfaces with neighboring surface-bound oxygen adsorbed onto CeO_2. Recently, Zheng et al. [21] confirmed by in situ diffuse-reflectance Fourier transform (DRIFT) analysis that the CO oxidation follows both the M-K and L-H mechanisms. On the one hand, the CeO_2 provides active sites for CO and O_2 chemisorption to form bicarbonate, unidentate carbonate and bidentate carbonate species for interactions; on the other hand, the lattice oxygen of the Ce-Zr solid solution reacts with the chemisorbed CO to form bridging carbonates. Although many studies have focused on the reaction mechanisms of CO oxidation, both the adsorption-reaction intermediates on various active sites and the dissimilar reaction pathways corresponding to the L-H and M-K mechanisms are unclear.

Therefore, in the present study, we prepared and characterized $CuO/Ce_{0.75}Zr_{0.25}O_{2-\delta}$, $Cu_{0.07}Ce_{0.75}Zr_{0.25}O_{2-\delta}$ and $Ce_{0.75}Zr_{0.25}O_\delta$ catalysts to investigate the physicochemical properties and the contributions of different active sites, which can determine their catalytic behavior. In particular, the chemisorption and active sites of the reactants and the reaction pathways were studied using in situ DRIFT and kinetics experiments. The results offer new insights into the active sites and reaction mechanisms of these catalysts.

2. Experiment specifications

2.1. Catalyst preparation

$Cu(NO_3)_2 \cdot 3H_2O$, $Ce(NO_3)_3 \cdot 6H_2O$ and $Zr(NO_3)_4 \cdot 5H_2O$ were combined in a 4:3:1 M ratio and dissolved fully in 70 mL of ethanol at 80 °C. This Cu:Ce:Zr ratio was selected on the basis of our previous study according to its good redox capability and oxygen storage capacity for CO oxidation [22,23]. Then, 0.24 mol/L of an oxalic acid solution was used as a pore former and was added quickly to the aforementioned nitrate solution with stirring to evaporate ethanol and to fully dissolve until a gel was formed at 80 °C over nearly 6 h. After aging at room temperature for approximately 48 h, the gel was dried at 105 °C for 12 h

and then calcined in air at 550 °C for 2 h. The obtained catalyst was labeled as $CuO/Ce_{0.75}Zr_{0.25}O_{2-\delta}$. To investigate the contribution of well-dispersed CuO active sites on the catalyst surface to CO oxidation, part of the $CuO/Ce_{0.75}Zr_{0.25}O_{2-\delta}$ catalyst was immersed and sonicated in concentrated nitric acid (15 mL of 50% HNO_3/g catalyst) for 2 h. This sample was then filtered and washed with a copious amount of distilled water to remove the residual HNO_3 and other impurities followed by drying at 120 °C. The resulting catalyst was labeled as $Cu_{0.07}Ce_{0.75}Zr_{0.25}O_{2-\delta}$. To compare the influence of different solid solutions on CO oxidation, $Ce(NO_3)_3 \cdot 6H_2O$ and $Zr(NO_3)_4 \cdot 5H_2O$ were reacted in a 3:1 mol ratio to prepare the $Ce_{0.75}Zr_{0.25}O_\delta$ catalyst using the same procedure as that used for $CuO/Ce_{0.75}Zr_{0.25}O_{2-\delta}$.

2.2. Characterizations

X-ray powder diffraction (XRD) analysis was performed on an XD-3-automatic (PERSEE) equipped with a Cu Kα radiation source (40 kV, 200 mA, λ = 1.5418 Å). The patterns were collected over the diffraction angle (2θ) range of 10° to 80° with a step length of 0.02° at a scanning rate of 4°/min. The elemental compositions of the catalysts were determined by X-ray fluorescence (XRF) analysis on an Epsilon l Research and a Power 4200 scanning XRF spectrometer. Transmission electron microscopy (TEM) images of the catalysts were observed on a JEM-2100 F electron microscope operating at 200 kV. Raman spectral analyses were performed on a HORIBA LabRAM HR Evolution spectrometer with a confocal microprobe Raman system. The spectrometer was equipped with 488 nm laser, a high-speed grating feedback platform (HSES) for the 100 nm step, a travel range of 112 mm × 76 mm, a spectral range of 10 cm^{-1} to 9000 cm^{-1}, a resolution of 1 cm^{-1}, and a light efficiency greater than 30%. X-ray photoelectron spectroscopy (XPS) was carried out on a Kratos Axis Ultra DLD spectrometer equipped with a monochromatic Al-Kα X-ray source and a delay line detector. The binding energy positions were normalized with the standard binding energy (284.8 eV, C1 s). Deconvolution of the peaks was performed by the XPS-Peak program after subtraction of the Shirley-type background using a sum of Lorentzian/Gaussian functions. N_2 adsorption-desorption isotherms were collected at −196 °C using an Autosorb-Iq-MP instrument (Quantachrome). The sample was degassed under a vacuum at 300 °C for more than 4 h before measurement. The specific surface area of the samples was calculated following the Brunauer-Emmett-Teller (BET) method. The average pore size was obtained by the Barrett-Joyner-Halenda (BJH) method and non-local density functional theory (NLDFT) modeling.

The temperature-programmed desorption of oxygen (O_2-TPD) was recorded on a PCA-140 instrument equipped with a TCD (Bolider). A 500 mg sample of fresh catalyst was used and adsorbed with O_2 at 50 °C for 1 h, cooled to 30 °C and then exposed to flowing He (30 mL/min); the reactor was heated to 1000 °C at a rate of 10 °C/min. H_2 temperature-programmed reduction (H_2-TPR) and N_2O chemisorption experiments were performed to investigate the redox ability and copper dispersion of the catalysts with a PCA-140 instrument [24,25]. Detailed procedures and the results of the H_2-TPR and N_2O decomposition are provided in Fig. S1 in the supporting information.

In situ DRIFT experiments were recorded on a Bruker Tensor 27 spectrometer. Self-supporting disks prepared from the sample powders were suspended in a quartz holder and then mounted in a high-temperature, high-pressure IR cell. Prior to the experiment, the sample (40 mg) was pretreated in He (80 mL/min) at 400 °C for 1 h and cooled to the desired temperature for collection of a reference spectrum. The reaction gas mixture (25 vol% CO + 25 vol% O_2, He balance) was fed to the sample at a total flow rate of 80 mL/min at room temperature for 0.5 h and then purged with He for 0.5 h to avoid the physical adsorption of CO/O_2. For each temperature interval (from room temperature to 500 °C), a series of time-dependent DRIFT spectra of the reaction on the sample were sequentially recorded with a resolution of 4 cm^{-1} and with the accumulation of 64 scans.

2.3. Catalytic activity testing

Catalytic activity was evaluated in a flow-type, temperature-controlled apparatus for continuous operation. The catalyst (200 mg, 0.1–0.15 mm) was loaded into a fixed-bed reactor made of a quartz tube with an inner diameter of 4 mm. The feed gas consisted of 1 vol% CO, 1 vol% O_2 and N_2 as balance with a total flow rate of 200 mL/min, corresponding to a 60,000 h^{-1} gas hourly space velocity (GHSV). The temperature-programmed oxidation (TPO) used a heating rate of 5 °C/min, and the K-type thermocouple was placed inside the center of the catalyst bed to measure the reaction temperature continuously. An online FTIR measurement system (QGS-08, Maihak) was used to monitor the effluent CO, O_2 and CO_2. Good reproducibility was found for the catalysts for each TPO experiment across three runs. To study the effect of H_2O in the CO catalytic reaction on catalysts, catalytic tests were performed by adding 1 vol% CO + 1 vol% O_2 + 5 vol% H_2O and N_2 as balance to the reactant gas mixture. The H_2O was introduced into the gas mixture by passing the gas stream through a gas saturator at 35 °C.

The kinetics experiments were studied with a CO conversion of less than 15% under a concentration of CO or O_2 in the feed gas ranging from 0.1 vol% to 3 vol%. The power-rate law expressions were obtained by taking the partial pressure of each reactant (kPa) and the reaction rate data and simultaneously fitting the entire dataset by a linear least squares regression analysis using the Polymath 5.1 program [26]. Detailed procedures of the kinetics experiments are provided in the supporting information.

3. Results

3.1. Structure properties

Fig. 1 shows the XRD patterns of the $CuO/Ce_{0.75}Zr_{0.25}O_{2-\delta}$, $Cu_{0.07}Ce_{0.75}Zr_{0.25}O_{2-\delta}$ and $Ce_{0.75}Zr_{0.25}O_{\delta}$ catalysts. The typical cubic fluorite structure of CeO_2 is observed in all three catalysts according to the peaks located at 28.5° and 47.4° (PDF No. 34-0394). Compared with the diffraction peaks in the pattern of cubic CeO_2, the diffraction peaks in the patterns of the three catalysts are broadened and shifted to higher 2θ values as a function of Cu and Zr addition, indicating lattice distortion in the cubic fluorite structure of CeO_2. Furthermore, two weak characteristic peaks at 2θ values of 35.5° and 38.7° show that bulk CuO crystallites are formed on the $CuO/Ce_{0.75}Zr_{0.25}O_{2-\delta}$ catalyst. However, the CuO phase on $Cu_{0.07}Ce_{0.75}Zr_{0.25}O_{2-\delta}$ was not detected because either the bulk CuO crystallites were removed or the crystallite size was below the detection limit (3 nm) of XRD.
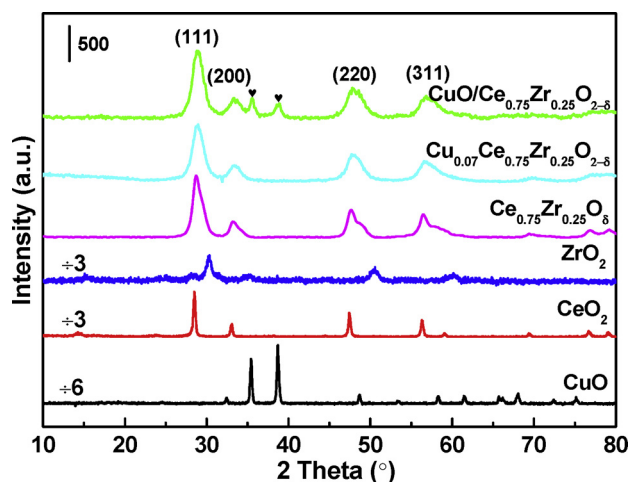
Fig. 1. Wide-angle XRD patterns of $CuO/Ce_{0.75}Zr_{0.25}O_{2-\delta}$, $Cu_{0.07}Ce_{0.75}Zr_{0.25}O_{2-\delta}$ and $Ce_{0.75}Zr_{0.25}O_{\delta}$ catalysts.

Table 1
Lattice parameters, average crystal sizes, 2θ, CuO contents and A_{628}/A_{463} ratios of $CuO/Ce_{0.75}Zr_{0.25}O_{2-\delta}$, $Cu_{0.07}Ce_{0.75}Zr_{0.25}O_{2-\delta}$ and $Ce_{0.75}Zr_{0.25}O_{\delta}$ catalysts.

Samples	Lattice parameter (nm)[a]	Average crystal size (nm)[a]	2θ(°) (111)[a]	Wt_{CuO} (%)[b]	A_{628}/A_{463}[c]
$CuO/Ce_{0.75}Zr_{0.25}O_{2-\delta}$	0.5369	5.069	28.9	33.38	0.402
$Cu_{0.07}Ce_{0.75}Zr_{0.25}O_{2-\delta}$	0.5374	5.165	28.9	3.63	0.518
$Ce_{0.75}Zr_{0.25}O_{\delta}$	0.5396	5.718	28.7	/	0.287
CeO_2	0.5411	5.901	28.5	/	0.040

[a] Determined by the XRD technique with the Rietveld method using the Jade 6.0 program.
[b] Determined by the XRF technique, where Wt_{CuO} (%) indicates the weight percent of CuO in the catalysts.
[c] Determined by the Raman technique, where A_{628}/A_{463} represents the ratio between the peak areas at 628 and 463 cm^{-1}.

The lattice parameters, average crystal size, CuO contents and diffraction peaks of catalysts are summarized in Table 1. The lattice parameters of $CuO/Ce_{0.75}Zr_{0.25}O_{2-\delta}$, $Cu_{0.07}Ce_{0.75}Zr_{0.25}O_{2-\delta}$ and $Ce_{0.75}Zr_{0.25}O_{\delta}$ are slightly smaller than that of pure CeO_2, with values of 0.5369 nm, 0.5374 nm, 0.5396 nm, and 0.5412 nm, respectively, displaying the same phenomenon as that for the average crystal size. Some Cu^{2+} ions (r_{Cu2+} = 0.072 nm) or Zr^{4+} ions (r_{Zr4+} = 0.084 nm) might be incorporated into the lattice of CeO_2 (r_{Ce4+} = 0.097 nm) to form new solid solutions [10]. As evident in the 2θ values in Table 1, ZrO_2 peaks are not observed in the XRD patterns of any of the three catalysts because of the dispersion of ZrO_2 and the easy formation Ce-Zr-O_{δ} solid solutions, as reported by Yang et al. [27]. With respect to the incorporation of CuO, Jia et al. found that surface CuO species can be removed by a nitric acid treatment, leaving a $Ce_{1-x}Cu_xO_{2-\delta}$ solid solution in the $CuO/Ce_{1-x}Cu_xO_{2-\delta}$ and $Ce_{1-x}Cu_xO_{2-\delta}$ catalysts [17]. In our study, the XRF data confirm that the CuO content remains at 3.63% for $Cu_{0.07}Ce_{0.75}Zr_{0.25}O_{2-\delta}$ although CuO crystallites can be removed by a nitric acid treatment. Changes in the 2θ values and the lattice parameters in $CuO/Ce_{0.75}Zr_{0.25}O_{2-\delta}$ and $Cu_{0.07}Ce_{0.75}Zr_{0.25}O_{2-\delta}$ suggest preliminarily that the residual CuO was likely inserted into the crystal lattice of CeO_2-ZrO_2 to form a Cu-Ce-Zr-O_{δ} solid solution; the formation of residual CuO should be further studied. The representative TEM images of the $CuO/Ce_{0.75}Zr_{0.25}O_{2-\delta}$, $Cu_{0.07}Ce_{0.75}Zr_{0.25}O_{2-\delta}$ and $Ce_{0.75}Zr_{0.25}O_{\delta}$ catalysts are listed in Fig. S2. This figure shows that no CuO particles are observed on the surface of $Cu_{0.07}Ce_{0.75}Zr_{0.25}O_{2-\delta}$, indicating that the particles were removed after the nitric acid treatment and that the residual Cu (3.63%) is embedded inside the subsurface of $Cu_{0.07}Ce_{0.75}Zr_{0.25}O_{2-\delta}$ to form a Cu-Ce-Zr-O_{δ} solid solution, which agrees with the XRD results. A detailed analysis is provided in the supporting information.

Raman spectra of the $CuO/Ce_{0.75}Zr_{0.25}O_{2-\delta}$, $Cu_{0.07}Ce_{0.75}Zr_{0.25}O_{2-\delta}$ and $Ce_{0.75}Zr_{0.25}O_{\delta}$ catalysts are shown in Fig. 2. The distinct band at approximately 463 cm^{-1} and the three weak bands at 290, 628 and 1188 cm^{-1} were observed in the spectra of all the catalysts. The bands at 290 and 628 cm^{-1} are ascribed to oxygen vacancies [28], whereas the weak band at 1188 cm^{-1} is ascribed to the primary A_{1g} asymmetry of CeO_2 [29]. The strong peaks at 463 cm^{-1} are attributed to the F_{2g} vibration mode of the fluorite structure of the pure CeO_2 and the Ce-Zr-O_{δ} solid solution, whereas the corresponding peaks in the spectra of the $CuO/Ce_{0.75}Zr_{0.25}O_{2-\delta}$ and $Cu_{0.07}Ce_{0.75}Zr_{0.25}O_{2-\delta}$ samples are shifted to lower frequencies (approximately 450 cm^{-1}) because of the formation of a Cu-Ce-Zr-O_{δ} solid solution [27]. The band at 628 cm^{-1} indicates the evolution of oxygen vacancies generated from different solid solutions and from the changes in the charge balance as a result of the partial replacement of Ce^{4+} ions by Cu^{2+} ions. The ratio between the areas of the peaks at 628 and 463 cm^{-1} (A_{628}/A_{463}) was used to determine the concentration of oxygen vacancies in these catalysts [4], as shown in Table 1.
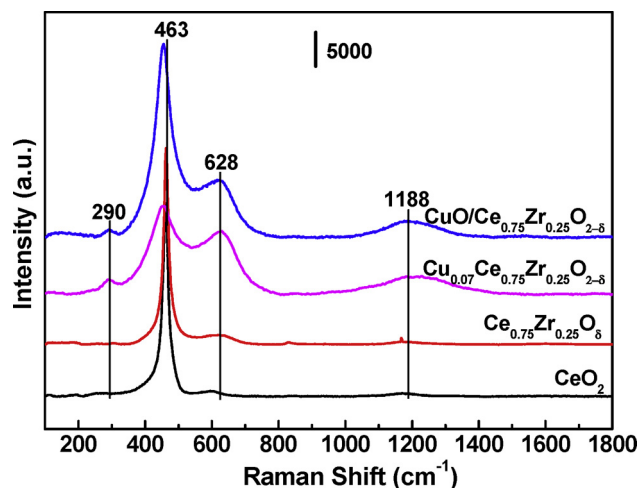
Fig. 2. Raman spectra of the $CuO/Ce_{0.75}Zr_{0.25}O_{2-\delta}$, $Cu_{0.07}Ce_{0.75}Zr_{0.25}O_{2-\delta}$ and $Ce_{0.75}Zr_{0.25}O_\delta$ catalysts.

The A_{628}/A_{463} value of $Ce_{0.75}Zr_{0.25}O_\delta$ is 0.287, which is higher than that of CeO_2 (0.04) because the ZrO_2 is incorporated into the CeO_2 lattice, causing lattice distortion and forming a Ce-Zr-O_δ solid solution. Additionally, the A_{628}/A_{463} value of $CuO/Ce_{0.75}Zr_{0.25}O_{2-\delta}$ (0.402) is lower than that of $Cu_{0.07}Ce_{0.75}Zr_{0.25}O_{2-\delta}$ (0.518), likely because of the partial removal of Ce^{4+} by the nitric acid treatment, which exposed more Ce^{3+}, resulting in the emergence of the weak band at $450\,cm^{-1}$. The A_{628}/A_{463} value for the $Ce_{0.75}Zr_{0.25}O_\delta$ catalyst is lower than that for the corresponding $CuO/Ce_{0.75}Zr_{0.25}O_{2-\delta}$ and $Cu_{0.07}Ce_{0.75}Zr_{0.25}O_{2-\delta}$ catalysts, implying that more oxygen vacancies are derived from the Cu-Ce-Zr-O_δ solid solution in the $CuO/Ce_{0.75}Zr_{0.25}O_{2-\delta}$ and $Cu_{0.07}Ce_{0.75}Zr_{0.25}O_{2-\delta}$ catalysts than those from the Ce-Zr-O_δ solid solution in the $Ce_{0.75}Zr_{0.25}O_\delta$ catalyst.

The N_2 adsorption-desorption isotherms and corresponding pore size distribution curves of the $CuO/Ce_{0.75}Zr_{0.25}O_{2-\delta}$, $Cu_{0.07}Ce_{0.75}Zr_{0.25}O_{2-\delta}$ and $Ce_{0.75}Zr_{0.25}O_\delta$ catalysts are shown in Fig. 3. Two curves with the same color and markers for each catalyst corresponding to the N_2 adsorption-desorption isotherm are shown in Fig. 3(a). The pore size distributions are calculated according to the

hysteresis loop formed by the two curves for each catalyst, as shown in Fig. 3(b). It is clear from Fig. 3(a) that $CuO/Ce_{0.75}Zr_{0.25}O_{2-\delta}$ shows type IV isotherms with an H3-type hysteresis loop according to the IUPAC classification, indicating the presence of mesopores. With respect to $Cu_{0.07}Ce_{0.75}Zr_{0.25}O_{2-\delta}$, typical type IV adsorption isotherms and a steep capillary condensation step with an H2-type hysteresis loop are clearly observed in Fig. 3(a), indicating the formation of worm-like mesopores in the catalyst. It is further demonstrated that mesopores are dominant in the $CuO/Ce_{0.75}Zr_{0.25}O_{2-\delta}$ (2.3–42.6 nm) in Fig. 3(b), while the pore size distribution curves of $Cu_{0.07}Ce_{0.75}Zr_{0.25}O_{2-\delta}$ and $Ce_{0.75}Zr_{0.25}O_\delta$ present a single narrow peak in the mesopore range from 2.1–18.6 nm and 2.6–8.3 nm, respectively, due to the small amount or absence of the CuO_x species. The BET surface area, pore volume, and mean pore size of the catalysts are also analyzed in Fig. 3. The surface area and pore volume of $CuO/Ce_{0.75}Zr_{0.25}O_{2-\delta}$ ($57.25\,m^2/g$, $0.14\,cm^3/g$) are lower than those of $Cu_{0.07}Ce_{0.75}Zr_{0.25}O_{2-\delta}$ ($105.26\,m^2/g$, $0.25\,cm^3/g$), while the mean pore size of $CuO/Ce_{0.75}Zr_{0.25}O_{2-\delta}$ (9.89 nm) is slightly higher than that of $Cu_{0.07}Ce_{0.75}Zr_{0.25}O_{2-\delta}$ (9.57 nm), and these differences are attributed to the presence of surface/bulk phase CuO_x species [13], which is in agreement with the TEM results.

The surface compositions and oxidation states of the different elements in the synthesized catalysts were characterized by XPS. The Cu 2p spectrum of $CuO/Ce_{0.75}Zr_{0.25}O_{2-\delta}$ shows two main peaks (Fig. 4A (a)): a peak at approximately 934.7 eV that can be assigned to Cu $2p_{3/2}$ and a peak at approximately 955 eV that can be attributed to Cu $2p_{1/2}$. The Cu $2p_{3/2}$ peak can be well fitted by two peaks at 934.2 and 936.2 eV, corresponding to the Cu^+ and Cu^{2+} ions, respectively [30]. The intense satellite peaks located in the range of 941.9–944.5 eV suggest the existence of divalent copper. In contrast, the Cu 2p peak cannot be observed in Fig. 4A (b), which is attributed to the removal of the dispersed CuO species and the CuO crystals from the CuO/$Ce_{0.75}Zr_{0.25}O_{2-\delta}$ surface by the nitric acid treatment, further confirming that the residual Cu ions (3.63%) are encapsulated in the CeO_2-ZrO_2 lattice, forming a Cu-Ce-Zr-O_δ solid solution on the subsurface of the $CuO/Ce_{0.75}Zr_{0.25}O_{2-\delta}$ and $Cu_{0.07}Ce_{0.75}Zr_{0.25}O_{2-\delta}$ catalysts, in agreement with other works [31,32].

Fig. 4B displays the Ce 3d XPS spectra of the (a) CuO/$Ce_{0.75}Zr_{0.25}O_{2-\delta}$, (b) $Cu_{0.07}Ce_{0.75}Zr_{0.25}O_{2-\delta}$ and (c) $Ce_{0.75}Zr_{0.25}O_\delta$ catalysts, which can be deconvoluted into $3d_{5/2}$ and $3d_{3/2}$ spin-orbit peaks (labeled as v and u, respectively) performing the $Ce^{3+} \leftrightarrow Ce^{4+}$
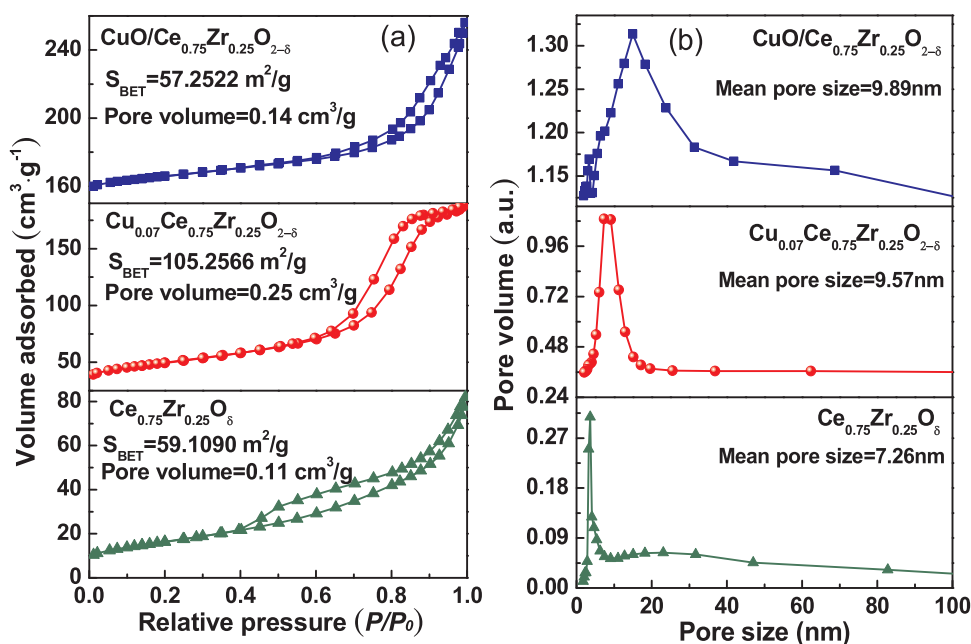
Fig. 3. N_2 adsorption and desorption isotherms (a) and pore size distributions (b) of the three catalysts.
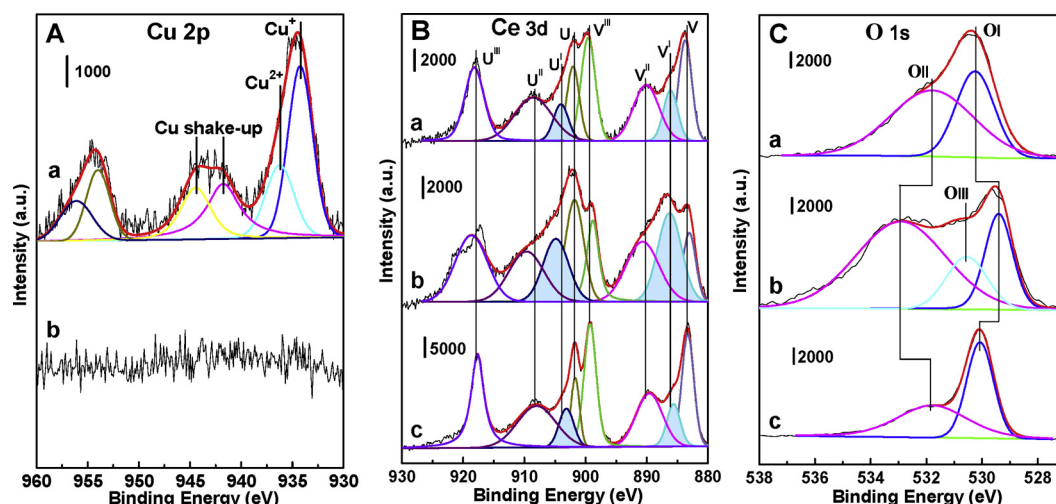
Fig. 4. XPS narrow spectra Cu 2p (A), Ce 3d (B) and O 1 s (C) over the (a) $CuO/Ce_{0.75}Zr_{0.25}O_{2-\delta}$, (b) $Cu_{0.07}Ce_{0.75}Zr_{0.25}O_{2-\delta}$ and (c) $Ce_{0.75}Zr_{0.25}O_\delta$ catalysts.

electronic transitions. The four intense peaks v (883.4 eV), u (902.0 eV), v^{III} (899.3 eV), and u^{III} (918.0 eV), as well as the two weaker peaks v^{II} (890.2 eV) and u^{II} (908.3 eV), can be attributed to different Ce 4f electron configurations in the final states of the Ce^{4+} species. The v^I (886.0 eV) and u^I (903.9 eV) components correspond to two possible electron configurations of the Ce^{3+} species in its final state [33].

The O 1 s XPS spectra of the three synthesized catalysts were resolved into two (a, c) and three peaks (b) by deconvolution, as shown in Fig. 4C. The OI (530.1 eV) peak is generally accepted as being a feature of the lattice oxygen (O_L) in cerium oxide, and the peak at OII (531.8 eV) is generally attributed to surface-adsorbed oxygen (O_S) for all the catalysts [30]. The OIII (530.7 eV) peak shown in Fig. 4C (b) represents the exposed surface oxygen resulting from the nitric acid treatment or surface hydroxyl species (OH_S).

The relative percentages of the Cu^{2+}/Cu^+, Ce^{3+}/Ce^{4+} and $O_L/(O_L + O_S)$ calculated according to the peak area ratios in the XPS spectra are listed in Table 2. The Cu^{2+}/Cu^+ ratio was measurable only in the case of the spectrum of the $CuO/Ce_{0.75}Zr_{0.25}O_{2-\delta}$ catalyst and had a value of 0.65, indicating that mostly Cu species are located on the catalyst surface. The ratio of Ce^{3+}/Ce^{4+} changes from 0.15 in $Cu_{0.07}Ce_{0.75}Zr_{0.25}O_{2-\delta}$ to 0.38 in $CuO/Ce_{0.75}Zr_{0.25}O_{2-\delta}$ because the exposed Ce^{3+} that partially replaces Ce^{4+} ions implies the formation of CeO_{2-x}, a defect structure that promotes the formation of oxygen vacancies by the nitric acid treatment, consistent with the Raman results [34]. Both the lattice oxygen (O_L) and the surface oxygen (O_S) are indispensable species for CO oxidation. As shown in Table 2, the ratio of $O_L/(O_L + O_S)$ decreases in the order of $Ce_{0.75}Zr_{0.25}O_\delta$ > $CuO/Ce_{0.75}Zr_{0.25}O_{2-\delta}$ > $Cu_{0.07}Ce_{0.75}Zr_{0.25}O_{2-\delta}$ because of the change in surface oxygen content.

3.2. Reducibility and oxygen mobility

The redox properties of the $CuO/Ce_{0.75}Zr_{0.25}O_{2-\delta}$, $Cu_{0.07}Ce_{0.75}Zr_{0.25}O_{2-\delta}$ and $Ce_{0.75}Zr_{0.25}O_\delta$ catalysts were analyzed by H_2-TPR. Fig. 5 shows three reduction peaks, labeled α (164 °C), β (210 °C) and γ (231 °C), for $CuO/Ce_{0.75}Zr_{0.25}O_{2-\delta}$ and one reduction peak,

Table 2
Surface atomic ratios of the $CuO/Ce_{0.75}Zr_{0.25}O_{2-\delta}$, $Cu_{0.07}Ce_{0.75}Zr_{0.25}O_{2-\delta}$ and $Ce_{0.75}Zr_{0.25}O_\delta$ catalysts obtained by XPS quantitative analysis.

Samples	Cu^{2+}/Cu^+	Ce^{3+}/Ce^{4+}	$O_L/(O_L+O_S)$
$CuO/Ce_{0.75}Zr_{0.25}O_{2-\delta}$	0.65	0.15	0.37
$Cu_{0.07}Ce_{0.75}Zr_{0.25}O_{2-\delta}$	/	0.38	0.21
$Ce_{0.75}Zr_{0.25}O_\delta$	/	0.12	0.50
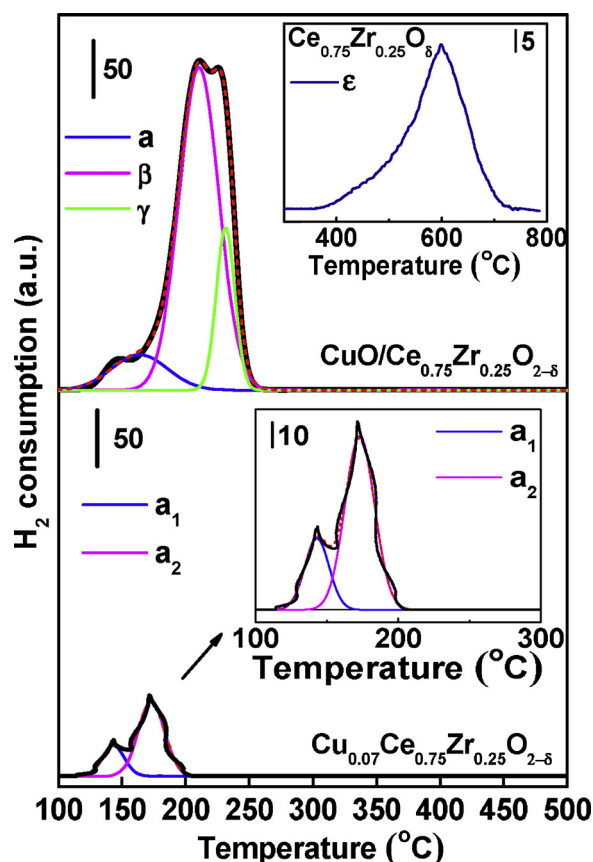
Fig. 5. H_2-TPR profiles of the $CuO/Ce_{0.75}Zr_{0.25}O_{2-\delta}$, $Cu_{0.07}Ce_{0.75}Zr_{0.25}O_{2-\delta}$ and $Ce_{0.75}Zr_{0.25}O_\delta$ catalysts.

labeled α ($α_1$ and $α_2$ corresponding to 143 °C and 172 °C) for $Cu_{0.07}Ce_{0.75}Zr_{0.25}O_{2-\delta}$ and ε (600 °C) for $Ce_{0.75}Zr_{0.25}O_\delta$. The reduction temperature of the $Ce_{0.75}Zr_{0.25}O_\delta$ catalysts ranges from 400 to 700 °C because of the poor redox properties of the Ce species, including surface CeO_2 and the Ce-Zr-O_δ solid solutions. For the reduction of the CuO_x species, an α peak at low temperatures is assigned to the reduction of CuO_x species in the Cu-Ce-Zr-O_δ solid solution that exhibit strong interactions with the Ce species in $CuO/Ce_{0.75}Zr_{0.25}O_{2-\delta}$ and $Cu_{0.07}Ce_{0.75}Zr_{0.25}O_{2-\delta}$. The β peak at moderate temperatures corresponds to the high dispersion of CuO_x species on the catalyst surface, and the γ peak at high temperatures exists only in the CuO/

Table 3

H$_2$ consumption, CuO dispersion (D) and TOF on the CuO/Ce$_{0.75}$Zr$_{0.25}$O$_{2-\delta}$ and Cu$_{0.07}$Ce$_{0.75}$Zr$_{0.25}$O$_{2-\delta}$ catalysts.

Samples	H$_2$ consumption (μmol·g^{-1})				D (%)	TOF$_a$ (s^{-1})	TOF$_b$ (s^{-1})
	α peak	β peak	γ peak	Total			
CuO/Ce$_{0.75}$Zr$_{0.25}$O$_{2-\delta}$	140 (164 °C)	908 (210 °C)	214 (231 °C)	1262	31.3	$(8.50 \pm 0.02) \times 10^{-4}$	$(1.38 \pm 0.02) \times 10^{-3}$
Cu$_{0.07}$Ce$_{0.75}$Zr$_{0.25}$O$_{2-\delta}$	187*	/	/	187	4.2	$(5.77 \pm 0.04) \times 10^{-2}$	$(6.95 \pm 0.05) \times 10^{-1}$

∗ α peak contains α_1 = 48 μmol·g^{-1} (143 °C) and α_2 = 139 μmol·g^{-1} (172 °C).

∗ D represents the dispersion (D) of CuO by the H$_2$-TPR + N$_2$O experiments.

∗ TOF represents the turnover frequency calculated by equations (5) and (6) in the supporting information.

Ce$_{0.75}$Zr$_{0.25}$O$_{2-\delta}$ catalyst and is attributed to the reduction of bulk CuO$_x$ [35–37]. Both the β and γ peaks disappear in Cu$_{0.07}$Ce$_{0.75}$Zr$_{0.25}$O$_{2-\delta}$ because the dispersed CuO species and bulk CuO$_x$ on the catalyst surface are easily removed by the nitric acid treatment, in agreement with the XRD and TEM analyses. Herein, the α peak can be attributed to the reduction of the Cu species in the subsurface of the CeO$_2$ lattice (Cu-Ce-Zr-O$_\delta$ solid solution) over the CuO/Ce$_{0.75}$Zr$_{0.25}$O$_{2-\delta}$ and Cu$_{0.07}$Ce$_{0.75}$Zr$_{0.25}$O$_{2-\delta}$ catalysts, which is also supported by the XPS and Raman results.

The reduction temperatures and the hydrogen consumption of the CuO$_x$ species as determined from the H$_2$-TPR profiles are listed in Table 3. The temperatures corresponding to the reduction peak of α (α_1 and α_2 peaks) in the profile of the Cu$_{0.07}$Ce$_{0.75}$Zr$_{0.25}$O$_{2-\delta}$ catalyst are slightly lower than those of the CuO/Ce$_{0.75}$Zr$_{0.25}$O$_{2-\delta}$ catalyst. The lower temperatures are likely due to the greater amount of exposed Ce^{3+} on the higher accessible surface area, which has a synergistic effect with the CuO species (Cu$^+$ and Cu^{2+}) to promote the reduction of CuO$_x$ species and expose surface Ce species, which is in agreement with the Raman and XPS results. The hydrogen consumption of the α peak on the CuO/Ce$_{0.75}$Zr$_{0.25}$O$_{2-\delta}$ catalyst is slightly lower than that on the Cu$_{0.07}$Ce$_{0.75}$Zr$_{0.25}$O$_{2-\delta}$ catalyst, in which the majority of the CuO$_x$ species in the Cu-Ce-Zr-O$_\delta$ solid solution over the CuO/Ce$_{0.75}$Zr$_{0.25}$O$_{2-\delta}$ and Cu$_{0.07}$Ce$_{0.75}$Zr$_{0.25}$O$_{2-\delta}$ catalysts and the very limited number of exposed surface Ce species interacting with CuO$_x$ species could be reduced (nearly 47 μmol·g^{-1}) over the Cu$_{0.07}$Ce$_{0.75}$Zr$_{0.25}$O$_{2-\delta}$ catalyst [17,38]. The hydrogen consumption of the β and γ peaks corresponds to the high content of Cu in the highly dispersed surface CuO$_x$ species and the bulk CuO$_x$ with larger particle sizes, respectively, and the hydrogen consumption values are higher than those of the α peak over the CuO/Ce$_{0.75}$Zr$_{0.25}$O$_{2-\delta}$ catalyst. It can be concluded that the greater accessible surface area and larger particle sizes promote the oxygen mobility and reducibility for the catalysts. However, differences in the CuO$_x$ contents caused the hydrogen consumption of CuO/Ce$_{0.75}$Zr$_{0.25}$O$_{2-\delta}$ to be higher than that of Cu$_{0.07}$Ce$_{0.75}$Zr$_{0.25}$O$_{2-\delta}$.

To further investigate the adsorption of oxygen on the CuO/Ce$_{0.75}$Zr$_{0.25}$O$_{2-\delta}$, Cu$_{0.07}$Ce$_{0.75}$Zr$_{0.25}$O$_{2-\delta}$ and Ce$_{0.75}$Zr$_{0.25}$O$_\delta$ catalysts, O$_2$-TPD measurements were conducted, and the results are illustrated in Fig. 6. The O$_2$ desorption peaks for all the catalysts can be divided into three parts: the low-temperature range (100–300 °C), the middle-temperature range (300–600 °C), and the high-temperature range (600–1100 °C). The low-temperature peak is attributed to the weakly adsorbed oxygen (O$_2$), the middle-temperature peak is related to the chemisorbed surface-active oxygen species (O$_2^-$/O$^-$), and the high-temperature peak is associated with the lattice oxygen (O^{2-}) that binds to metal cations [21]. Notably, the intensity of the middle-temperature peak for Cu$_{0.07}$Ce$_{0.75}$Zr$_{0.25}$O$_{2-\delta}$ is higher than that for the CuO/Ce$_{0.75}$Zr$_{0.25}$O$_{2-\delta}$ catalyst, whereas the intensity of the high-temperature peak for the former is far lower than that for the latter. The higher accessible surface area and concentration of Ce^{3+} likely increase the amount of chemisorbed oxygen and promote the fast migration of more lattice oxygen species to the surface of Cu$_{0.07}$Ce$_{0.75}$Zr$_{0.25}$O$_{2-\delta}$, indicating a relatively high lattice oxygen mobility [39].
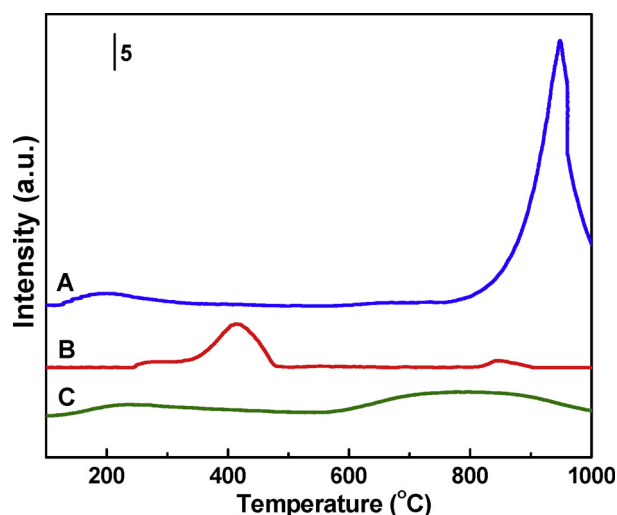
Fig. 6. O$_2$-TPD profiles of the (A) CuO/Ce$_{0.75}$Zr$_{0.25}$O$_{2-\delta}$, (B) Cu$_{0.07}$Ce$_{0.75}$Zr$_{0.25}$O$_{2-\delta}$ and (C) Ce$_{0.75}$Zr$_{0.25}$O$_\delta$ catalysts.

3.3. Catalytic activity testing

Fig. 7 and Table 4 show the CO oxidation activity over the CuO/Ce$_{0.75}$Zr$_{0.25}$O$_{2-\delta}$, Cu$_{0.07}$Ce$_{0.75}$Zr$_{0.25}$O$_{2-\delta}$ and Ce$_{0.75}$Zr$_{0.25}$O$_\delta$ catalysts. In Fig. 7(A) and (B), the T$_{10}$ and T$_{90}$ values (corresponding to 10% and 90% CO conversion, respectively) for CuO/Ce$_{0.75}$Zr$_{0.25}$O$_{2-\delta}$ are 90 and 150 °C, respectively, which are lower than those of Cu$_{0.07}$Ce$_{0.75}$Zr$_{0.25}$O$_{2-\delta}$ (T$_{10}$ = 135 °C, T$_{90}$ = 210 °C), indicating that the activity of well-dispersed CuO species is higher than that of a Cu-Ce-Zr-O$_\delta$ solid solution in the catalyst. Compared with the T$_{90}$ value for Cu$_{0.07}$Ce$_{0.75}$Zr$_{0.25}$O$_{2-\delta}$ (210 °C) and Ce$_{0.75}$Zr$_{0.25}$O$_\delta$ (365 °C), the results confirm that the activity of the Cu-Ce-Zr-O$_\delta$ solid solution is higher than that of the Ce-Zr-O$_\delta$ solid solution. Hence, the catalytic activity of the catalysts decreases in the following order: CuO/Ce$_{0.75}$Zr$_{0.25}$O$_{2-\delta}$ > Cu$_{0.07}$Ce$_{0.75}$Zr$_{0.25}$O$_{2-\delta}$ > Ce$_{0.75}$Zr$_{0.25}$O$_\delta$. Therefore, the reaction sensitivity of the CO oxidation process follows the order of CuO species > Cu-Ce-Zr-O$_\delta$ solid solution > Ce-Zr-O$_\delta$ solid solution. Fig. 7(C) and (D) show the CO oxidation with 5 vol.% H$_2$O. It can be seen that the curves of the activities shift toward higher temperatures, suggesting that the external chemisorption of H$_2$O on the catalysts is expected to compete with CO chemisorption. The textural characteristics of the catalysts (including high surface area and pore volume) promote the external chemisorption of H$_2$O. H$_2$O chemisorption into the channels also increases the amount of structural water, thus decreasing the quantity of oxygen vacancies and oxygen mobility. Nevertheless, the CO can be completely converted into CO$_2$ according to 2CO + O$_2$→2CO$_2$, with the same tendency as that without H$_2$O addition.

Fig. 8 displays the normalized rates for CO oxidation in the kinetic region of Fig. 6(A) (the kinetic region was determined in section 3.5) over CuO/Ce$_{0.75}$Zr$_{0.25}$O$_{2-\delta}$, Cu$_{0.07}$Ce$_{0.75}$Zr$_{0.25}$O$_{2-\delta}$ and Ce$_{0.75}$Zr$_{0.25}$O$_\delta$ catalysts. The normalized reaction rates and reaction temperature
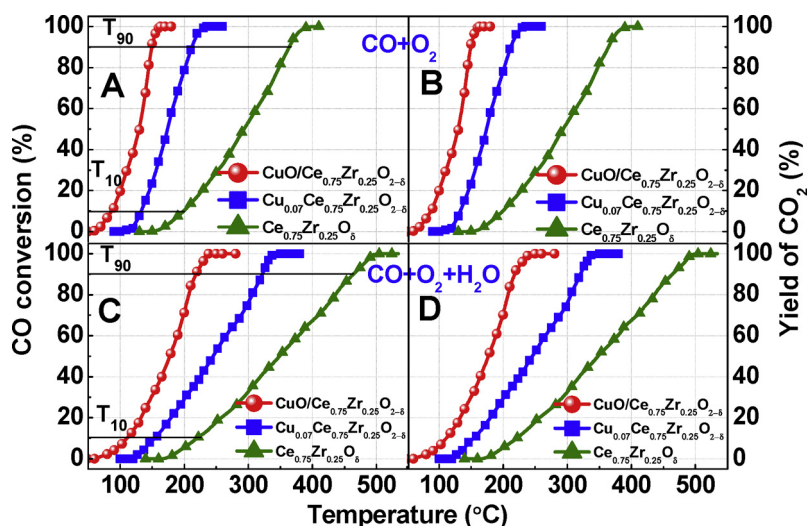
Fig. 7. CO oxidation with the $CuO/Ce_{0.75}Zr_{0.25}O_{2-\delta}$, $Cu_{0.07}Ce_{0.75}Zr_{0.25}O_{2-\delta}$ and $Ce_{0.75}Zr_{0.25}O_{\delta}$ catalysts under gas mixtures of different compositions (A and B in 1 vol. % CO + 1 vol.% O_2 / N_2 balance, C and D in 1 vol.% CO + 1 vol.% O_2 + 5 vol.% H_2O / N_2 balance).

Table 4

Catalytic activities of different catalysts under different gas mixtures.

Samples	1 vol.% CO + 1 vol.% O_2		1 vol.% CO + 1 vol.% O_2 + 5 vol.% H_2O	
	T_{10} (°C)	T_{90} (°C)	T_{10} (°C)	T_{90} (°C)
$CuO/Ce_{0.75}Zr_{0.25}O_{2-\delta}$	90 ± 1	150 ± 2	110 ± 1	218 ± 1
$Cu_{0.07}Ce_{0.75}Zr_{0.25}O_{2-\delta}$	135 ± 2	210 ± 1	156 ± 1	320 ± 2
$Ce_{0.75}Zr_{0.25}O_{\delta}$	200 ± 1	365 ± 1	220 ± 2	465 ± 1
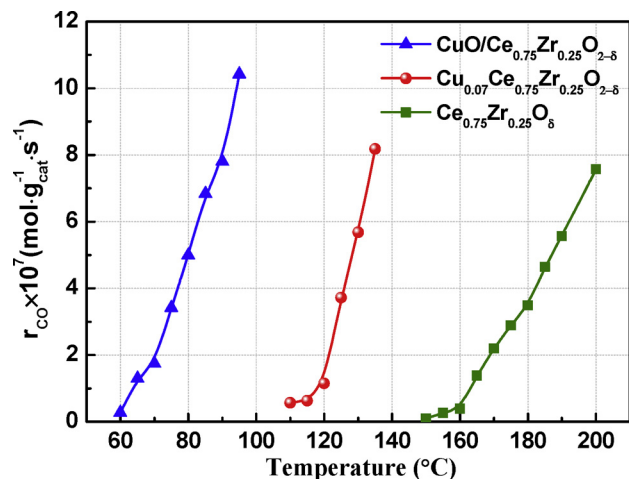
Fig. 8. The normalized rates for CO oxidation over $CuO/Ce_{0.75}Zr_{0.25}O_{2-\delta}$, $Cu_{0.07}Ce_{0.75}Zr_{0.25}O_{2-\delta}$ and $Ce_{0.75}Zr_{0.25}O_{\delta}$ catalysts.

regions are $0.28–10.42 \times 10^{-7}$ (60–95 °C), $0.57–8.18 \times 10^{-7}$ (110–135 °C), and $0.01–7.57 \times 10^{-7}$ (150–200 °C) $mol \cdot g_{cat}^{-1} \cdot s^{-}$ for the $CuO/Ce_{0.75}Zr_{0.25}O_{2-\delta}$, $Cu_{0.07}Ce_{0.75}Zr_{0.25}O_{2-\delta}$ and $Ce_{0.75}Zr_{0.25}O_{\delta}$ catalysts, respectively. The normalized rate values increase almost monotonously with temperature for the catalysts tested. The CuO/$Ce_{0.75}Zr_{0.25}O_{2-\delta}$ catalyst shows a significantly higher normalized reaction rate per unit mass and time at lower temperature regions compared with the lower normalized reaction rate per unit mass and time at higher temperature regions for the $Ce_{0.75}Zr_{0.25}O_{\delta}$ catalyst, indicating that the reaction sensitivity of the CO oxidation process follows the order of $CuO/Ce_{0.75}Zr_{0.25}O_{2-\delta} > Cu_{0.07}Ce_{0.75}Zr_{0.25}O_{2-\delta} > Ce_{0.75}Zr_{0.25}O_{\delta}$, which corresponds to the temperature range of 60–95 °C,
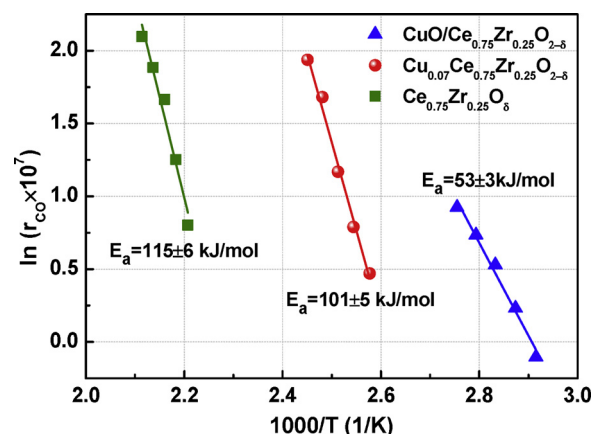
Fig. 9. Arrhenius plots for CO oxidation over $CuO/Ce_{0.75}Zr_{0.25}O_{2-\delta}$, $Cu_{0.07}Ce_{0.75}Zr_{0.25}O_{2-\delta}$ and $Ce_{0.75}Zr_{0.25}O_{\delta}$ catalysts.

110–135 °C, and 150–200 °C, respectively.

Fig. 9 presents the Arrhenius plots of the CO reaction rates in the kinetic region over the $CuO/Ce_{0.75}Zr_{0.25}O_{2-\delta}$, $Cu_{0.07}Ce_{0.75}Zr_{0.25}O_{2-\delta}$ and $Ce_{0.75}Zr_{0.25}O_{\delta}$ catalysts. The activation energies of CO oxidation for these catalysts are calculated as 53 ± 3 ($CuO/Ce_{0.75}Zr_{0.25}O_{2-\delta}$, $R^2 = 0.984$), 105 ± 5 ($Cu_{0.07}Ce_{0.75}Zr_{0.25}O_{2-\delta}$, $R^2 = 0.988$) and 115 ± 6 kJ/mol ($Ce_{0.75}Zr_{0.25}O_{\delta}$, $R^2 = 0.964$), which are similar to the range of activation energies previously reported for CO oxidation over $CuO/Ce_{1-x}Cu_xO_2\text{-}\delta$ (42 kJ/mol), $Ce_{1-x}Cu_xO_{2-\delta}$ (95 kJ/mol) and CeO_2-ZrO_2 (57–137 kJ/mol) catalysts [17,21]. These activation energies of CO oxidation reveal that the catalytic activities follow the order of $CuO/Ce_{0.75}Zr_{0.25}O_{2-\delta} > Cu_{0.07}Ce_{0.75}Zr_{0.25}O_{2-\delta} > Ce_{0.75}Zr_{0.25}O_{\delta}$.

Comparing the Cu-Ce-Zr mass-normalized rates for the CO oxidation reaction with the previously results reported for the CO reaction over standard catalysts (see Table 5), the $CuO/Ce_{0.75}Zr_{0.25}O_{2-\delta}$ catalyst achieves reaction rates of 7.81×10^{-7} $mol \cdot g_{cat}^{-1} \cdot s^{-1}$ at a reaction temperature of 90 °C, which is a higher rate than that of $CuO/Ce_{1-x}Cu_xO_{2-\delta}$-5 for $7.74 \times 10^{-7} mol \cdot g_{cat}^{-1} \cdot s^{-1}$ [17], $CuO/Ce_{0.6}Zr_{0.4}O_2$ for 2.18×10^{-7} $mol \cdot g_{cat}^{-1} \cdot s^{-1}$ [27], and $Ce_{0.95}Cu_{0.05}O_{2-\delta}$ for 1.43×10^{-7} $mol \cdot g_{cat}^{-1} \cdot s^{-1}$ [24] under similar reaction conditions.

3.4. In situ DRIFT of the CO interaction with O_2

DRIFT spectra were obtained to investigate the co-adsorption and reaction behavior of CO/O_2 on the $CuO/Ce_{0.75}Zr_{0.25}O_{2-\delta}$,

Table 5

Reaction rates of the CO oxidation reaction over different catalysts and the respective reaction conditions.

Samples	Temperature (°C)	Reaction gas mixture	Rate × 10^7 (mol·g$_{cat}^{-1}$·s^{-1})	Reference
CuO/Ce$_{0.75}$Zr$_{0.25}$O$_{2-\delta}$	90	1%CO + 1%O$_2$, rest N$_2$	7.81 ± 0.08	This work
CuO/Ce$_{1-x}$Cu$_x$O$_{2-\delta}$-5	90	1%CO + 1%O$_2$, rest N$_2$	7.74 ± 0.14	[17]
CuO/Ce$_{0.6}$Zr$_{0.4}$O$_2$	90	1%CO + 1%O$_2$, rest N$_2$	2.18 ± 0.06	[27]
Ce$_{0.95}$Cu$_{0.05}$O$_{2-\delta}$	90	1%CO + 1%O$_2$, rest N$_2$	1.43 ± 0.09	[24]
Cu$_{0.07}$Ce$_{0.75}$Zr$_{0.25}$O$_{2-\delta}$	130	1%CO + 1%O$_2$, rest N$_2$	5.68 ± 0.11	This work
Ce$_{1-x}$Cu$_x$O$_{2-\delta}$-5	160	1%CO + 1%O$_2$, rest N$_2$	4.17 ± 0.13	[17]
Ce$_{0.75}$Zr$_{0.25}$O$_\delta$	190	1%CO + 1%O$_2$, rest N$_2$	5.57 ± 0.15	This work
CeO$_2$-ZrO$_2$-600	190	1%CO + 10%O$_2$, rest He	2.23 ± 0.07	[21]
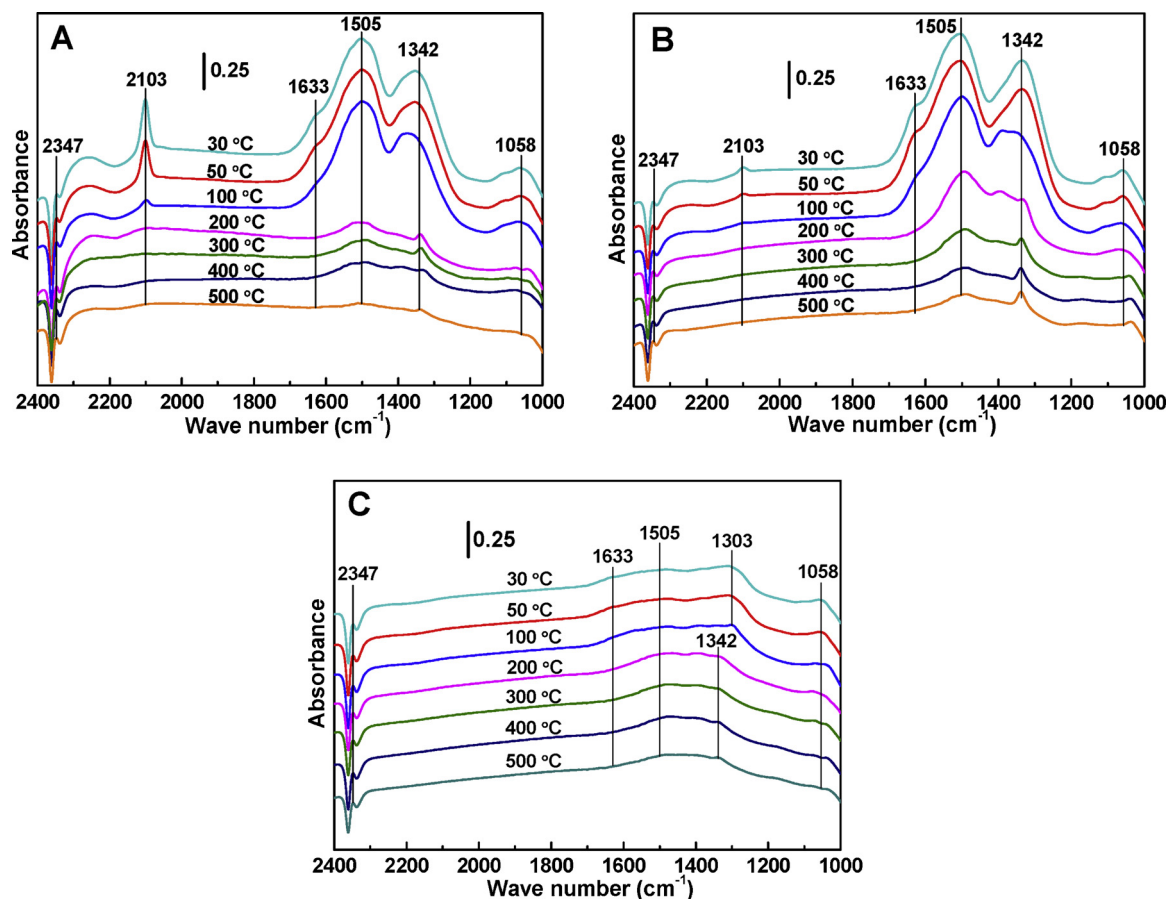
Fig. 10. In situ DRIFT spectra for the CO/O$_2$ co-adsorption and reaction over the three catalysts: (A) CuO/Ce$_{0.75}$Zr$_{0.25}$O$_{2-\delta}$, (B) Cu$_{0.07}$Ce$_{0.75}$Zr$_{0.25}$O$_{2-\delta}$ and (C) Ce$_{0.75}$Zr$_{0.25}$O$_\delta$ (25 vol.% CO + 25 vol.% O$_2$, He balance).

Table 6

The IR band initial areas of different carbonyl and carbonate species after CO adsorption at 30 °C.

Samples	IR band initial area			
	2103 cm^{-1}	1505 + 1058 cm^{-1}	1342 cm^{-1}	1633 cm^{-1}
CuO/Ce$_{0.75}$Zr$_{0.25}$O$_{2-\delta}$	10.4 ± 0.2	148.2 ± 0.8	99.0 ± 0.3	24.4 ± 0.3
Cu$_{0.07}$Ce$_{0.75}$Zr$_{0.25}$O$_{2-\delta}$	1.3 ± 0.1	170.0 ± 1.0	119.0 ± 0.7	34.7 ± 0.2
Ce$_{0.75}$Zr$_{0.25}$O$_\delta$	0.2 ± 0	43.4 ± 0.4	40.0 ± 0.4	7.8 ± 0.2

Cu$_{0.07}$Ce$_{0.75}$Zr$_{0.25}$O$_{2-\delta}$ and Ce$_{0.75}$Zr$_{0.25}$O$_\delta$ catalysts; the results are shown in Fig. 10.

Three major types of carbonate species are detected in the CO/O$_2$ co-adsorption process because of the interaction between CO and surface oxygen on the different catalysts: a bidentate carbonate species (1058 and 1505 cm^{-1}), a unidentate carbonate species (1303 and 1342 cm^{-1}) and a bicarbonate species (1633 cm^{-1}) [21]. Bands in the

2000–2200 cm^{-1} region are generally accepted to be associated with linearly bonded CO molecules interacting with Cu sites via the back donation of electrons from the catalyst surface cations into the antibonding π-orbital [18]. Thus, the band at 2103 cm^{-1} is assigned to the C−O stretching mode of Cu$^+$−CO on CuO/Ce$_{0.75}$Zr$_{0.25}$O$_{2-\delta}$ and Cu$_{0.07}$Ce$_{0.75}$Zr$_{0.25}$O$_{2-\delta}$, implying activation of the C−O bond by surface adsorption onto CuO species and suggesting that CuO species are the

main active sites for CO oxidation [11]. The bands at 2347 cm^{-1} are related to the CO_2 originating from the oxidation of Cu^+-CO and to the decomposition of carbonate species. By contrast, the CO_2 signal (2347 cm^{-1}) changed monotonically with increasing temperature.

The IR band initial areas of different carbonyl and carbonate species at 30 °C are also listed in Table 6. The IR band initial area of the 2103 cm^{-1} band for $CuO/Ce_{0.75}Zr_{0.25}O_{2-\delta}$ (10.4) is much higher than that of $Cu_{0.07}Ce_{0.75}Zr_{0.25}O_{2-\delta}$ (1.3) and $Ce_{0.75}Zr_{0.25}O_{\delta}$ (0.2) since the surface CuO species contribute to this adsorption. The IR band initial areas of the carbonate species peaks (1505 + 1058, 1342 and 1633 cm^{-1}) for $Ce_{0.75}Zr_{0.25}O_{\delta}$ are far lower than those of $CuO/Ce_{0.75}Zr_{0.25}O_{2-\delta}$ and $CuCe_{0.75}Zr_{0.25}O_{\delta}$ (H), implying that it is more difficult for the Ce-Zr-O_{δ} solid solution in $Ce_{0.75}Zr_{0.25}O_{\delta}$ to adsorb CO and O_2 than for the Cu-Ce-Zr-O_{δ} solid solution in $CuO/Ce_{0.75}Zr_{0.25}O_{2-\delta}$ and $Cu_{0.07}Ce_{0.75}Zr_{0.25}O_{2-\delta}$ to adsorb CO and O_2. Additionally, the IR band initial areas of the carbonate peaks for $Cu_{0.07}Ce_{0.75}Zr_{0.25}O_{2-\delta}$ are stronger than those for $CuO/Ce_{0.75}Zr_{0.25}O_{2-\delta}$ because more Ce^{3+} exposed after the nitric acid treatment promotes O_2 chemisorption and possesses a higher surface area to chemisorb CO/O_2, thus forming more carbonate species on the surface of $Cu_{0.07}Ce_{0.75}Zr_{0.25}O_{2-\delta}$. The IR band area change per unit mass and time (IRAQT, $\Delta A \cdot g_{cat}^{-1} \cdot s^{-1}$) versus temperature plots are also employed to determine the reaction rates of the carbonyl and carbonate species to obtain quantitative results (Fig. S3 in the supporting information). The values of IRAQT indicated that the Cu^+-CO species first reacts and decomposes quickly to generate CO_2 at temperatures ≤ 100 °C, followed by the decomposition of carbonate species to form CO_2 at ≥100 °C. According to the aforementioned results, the catalytic activity of the active sites decreases as follows: surface CuO species > Cu-Ce-Zr-O_{δ} solid solution > Ce-Zr-O_{δ} solid solution. This phenomenon is consistent with the normalized reaction rates for CO oxidation (see Fig. 8).

3.5. Kinetic study

To eliminate both internal and external mass transfer resistance, separate experiments were conducted; their results are shown in Fig. 11. Herein, the value of m/q ≤ 2 (a gas flow rate higher than 150 mL/min) can eliminate external mass transfer resistance with the same CO conversion (Fig. 11A). Catalyst particles that are smaller than 0.15–0.2 mm can maintain the CO conversion rate (8.7%) to eliminate internal mass transfer resistance (Fig. 11B). Hence, the appropriate gas flow rate (200 mL/min) and catalyst particle size (0.1–0.15 mm) with 0.2 g of catalyst are employed for the kinetic study. The absence of mass transport resistance was also confirmed by the Weisz-Prater criterion for internal diffusion and by the Mears criterion for external diffusion, and the absence of heat transfer was confirmed by the Mears criterion

[40] (the detailed calculation is shown in the supplementary information). The following values were calculated for the $CuO/Ce_{0.75}Zr_{0.25}O_{2-\delta}$ catalyst: the Weisz-Prater criterion is 1.14×10^{-3} for internal diffusion, the Mears criterion is 2.26×10^{-3} for external diffusion, and the Mears criterion is 0.075 for heat transfer under kinetic conditions. The calculated values for the $Cu_{0.07}Ce_{0.75}Zr_{0.25}O_{2-\delta}$ and $Ce_{0.75}Zr_{0.25}O_{\delta}$ catalysts are as follows: the Weisz-Prater criteria are 2.03×10^{-3} and 1.9×10^{-3} for internal diffusion, respectively, the Mears criteria are 2.56×10^{-3} and 2.4×10^{-3} for external diffusion, respectively, and the Mears criteria are 0.1 and 0.076 for heat transfer under kinetic conditions, respectively. These results ensure plug flow and isothermal conditions in the fixed bed reactor.

The kinetic data of the CO reaction rates under various partial pressures of CO and O_2 as well as the parity plots comparing the experimental rates with the calculated rates via data fitting are shown for all the catalysts in Fig. 12. Reaction temperatures (T_{10}) of 90, 135 and 200 °C are employed to account for the different catalytic performances of the $CuO/Ce_{0.75}Zr_{0.25}O_{2-\delta}$, $Cu_{0.07}Ce_{0.75}Zr_{0.25}O_{2-\delta}$ and $Ce_{0.75}Zr_{0.25}O_{\delta}$ catalysts, respectively. For all three catalysts, the reaction rates obviously increase as either the partial pressure of CO or the partial pressure of O_2 increases, as shown in Fig. 12(A), (B), and (C). The power-rate law of the reaction rates were obtained using the Polymath 5.1 program on the basis of the kinetics results as follows: $r = 6.02 \times 10^{-7} \times P_{CO}^{0.68}P_{O2}^{0.03}$ for $CuO/Ce_{0.75}Zr_{0.25}O_{2-\delta}$, $r = 5.86 \times 10^{-7} \times P_{CO}^{0.8}P_{O2}^{0.07}$ for $Cu_{0.07}Ce_{0.75}Zr_{0.25}O_{2-\delta}$ and $r = 5.7 \times 10^{-7} \times P_{CO}^{0.75}P_{O2}^{0.12}$ for $Ce_{0.75}Zr_{0.25}O_{\delta}$. These expressions indicate that the CO oxidation may occur through different reaction pathways over the three different catalysts. Fig. 12(D) shows that the fitted lines of the parity plots of the three catalysts pass through the origin and have no systematic deviations, implying that the regression is accurate.

The elementary steps considered in the kinetic models (both M-K and L-H models) of CO oxidation are proposed for the $CuO/Ce_{0.75}Zr_{0.25}O_{2-\delta}$, $Cu_{0.07}Ce_{0.75}Zr_{0.25}O_{2-\delta}$ and $Ce_{0.75}Zr_{0.25}O_{\delta}$ catalysts. The M-K model involves CO chemisorption on Cu^+ ions of the surface CuO to form Cu^+ carbonyl species, which can further interact with lattice oxygen provided by the Cu-Ce-Zr-O_{δ} solid solution. Then, gas-phase O_2 refills the oxygen vacancies to complete the CO oxidation reaction. The elementary reaction steps are as follows:

$$CO + Cu^+ \leftrightarrow Cu^+\text{-}CO \tag{1}$$

$$Cu^+\text{-}CO + Cu^{2+}\text{-}[O^{2-}]\text{-}Ce^{4+} \rightarrow Cu^+ + Cu^+\text{-}[]\text{-}Ce^{3+} + CO_2 \tag{2}$$

$$O_2 + 2Cu^+\text{-}[]\text{-}Ce^{3+} \leftrightarrow 2Cu^{2+}\text{-}[O^{2-}]\text{-}Ce^{4+} \tag{3}$$
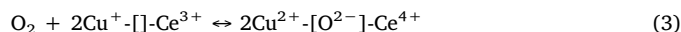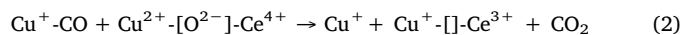
The reaction rate expression is based on the elementary step results:
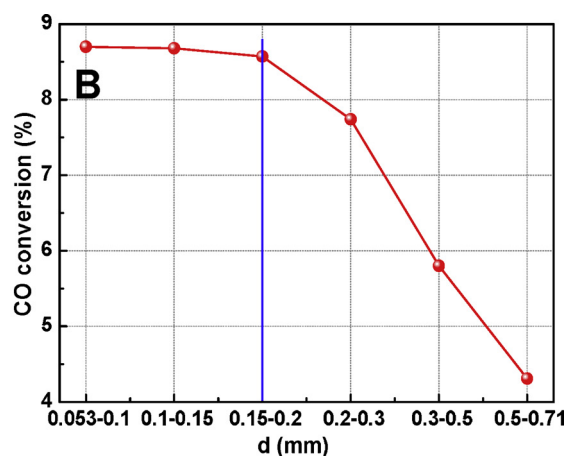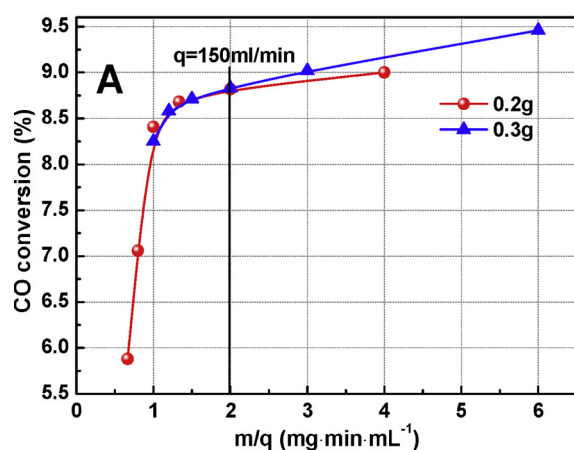
Fig. 11. The separate experiments of (A) external diffusion resistance and (B) internal diffusion resistance over the $CuO/Ce_{0.75}Zr_{0.25}O_{2-\delta}$ catalyst (1 vol.% CO + 1 vol.% O_2/ N_2).
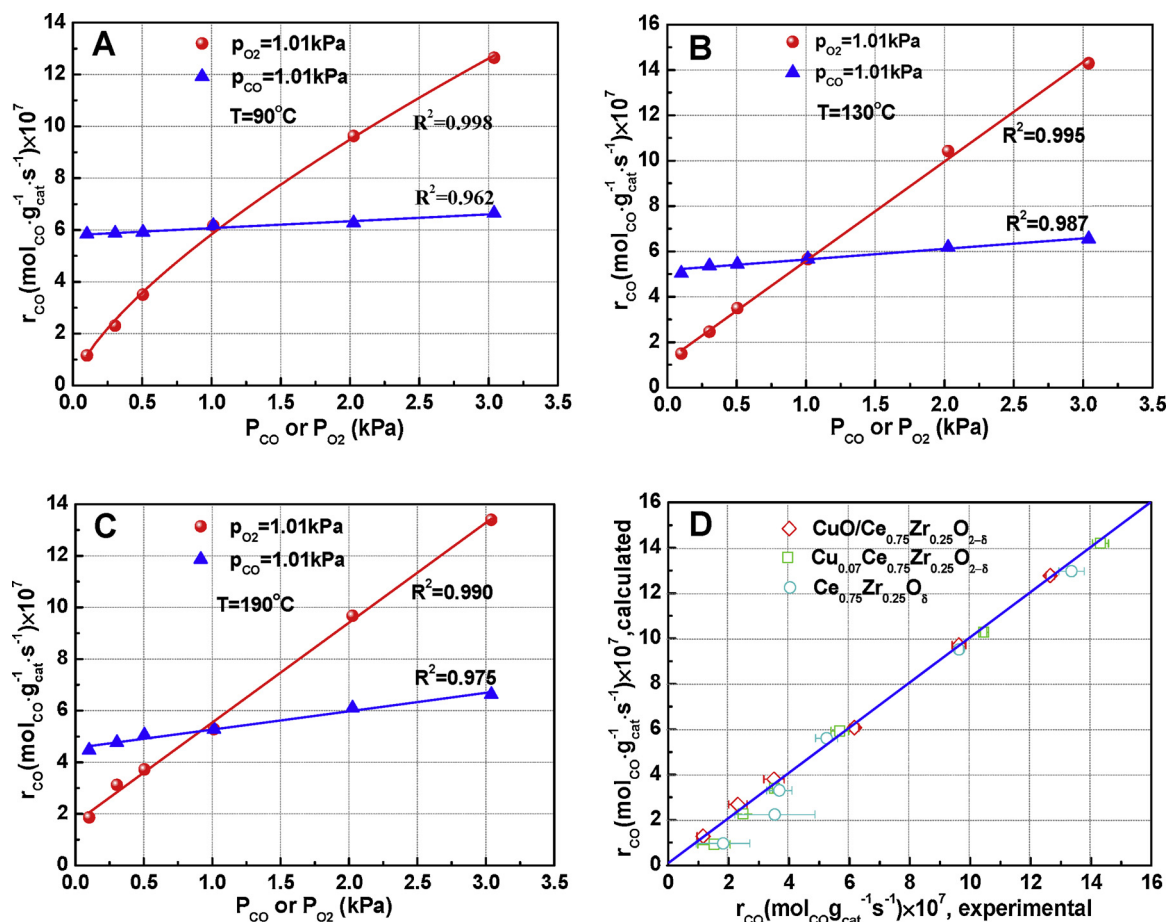
Fig. 12. Kinetic results of CO oxidation over the (A) $CuO/Ce_{0.75}Zr_{0.25}O_{2-\delta}$, (B) $Cu_{0.07}Ce_{0.75}Zr_{0.25}O_{2-\delta}$, (C) $Ce_{0.75}Zr_{0.25}O_{\delta}$ catalysts and (D) parity plots of CO reaction rates.

$$r = k_1 k_2 [O^{2-}] \frac{P_{CO}}{1 + k_1 P_{CO}} \tag{4}$$

where $[O^{2-}]$ refers to lattice oxygen, and [] refers to an oxygen vacancy.

The basic assumptions for CO oxidation are as follows: (1) CO chemisorption occurs on Cu^+ ions of surface CuO to form Cu^+ carbonyl species over $CuO/Ce_{0.75}Zr_{0.25}O_{2-\delta}$, $Cu_{0.07}Ce_{0.75}Zr_{0.25}O_{2-\delta}$ (Eq. (1)). (2) The chemisorbed CO migrates to the interface of the CuO and Cu-Ce-Zr-O_δ solid solution and reacts with lattice oxygen provided by Cu-Ce-Zr-O_δ, which can be considered as the rate-determining step (RDS) (Eq. (2)). (3) The gas-phase O_2 refills oxygen vacancies from the Cu-Ce-Zr-O_δ or Ce-Zr-O_δ solid solution to form lattice oxygen. (4) The chemisorption of CO on active site CuO was evidenced by the in situ DRIFT results.

The L-H model involves the chemisorption of CO and O_2 on the Cu-Ce-Zr-O_δ solid solution over the $CuO/Ce_{0.75}Zr_{0.25}O_{2-\delta}$ and $Cu_{0.07}Ce_{0.75}Zr_{0.25}O_{2-\delta}$ catalysts or the Ce-Zr-O_δ solid solution over the $Ce_{0.75}Zr_{0.25}O_\delta$ catalyst, thus forming three major types of carbonate species (bidentate carbonate, unidentate carbonate, and bicarbonate), which then decompose with increasing temperature. The elementary reaction steps are listed as follows.

For $CuO/Ce_{0.75}Zr_{0.25}O_{2-\delta}$ and $Cu_{0.07}Ce_{0.75}Zr_{0.25}O_{2-\delta}$:

$$CO + Cu^{2+}\text{-}Ce^{4+} + O_2 + \square \leftrightarrow CO\text{-}Cu^{2+}\text{-}Ce^{4+}\text{-}O_2 \tag{5}$$

$$CO\text{-}Cu^{2+}\text{-}Ce^{4+}\text{-}O_2 \rightarrow Cu^{2+}\text{-}Ce^{4+} + CO_2 \tag{6}$$

For $Ce_{0.75}Zr_{0.25}O_\delta$:

$$CO + Ce^{4+}\text{-}Zr^{4+} + O_2 + \square \leftrightarrow CO\text{-}Ce^{4+}\text{-}Zr^{4+}\text{-}O_2 \tag{7}$$

$$CO\text{-}Ce^{4+}\text{-}Zr^{4+}\text{-}O_2 \rightarrow Ce^{4+}\text{-}Zr^{4+} + CO_2 \tag{8}$$
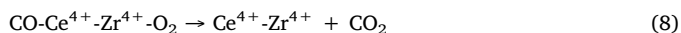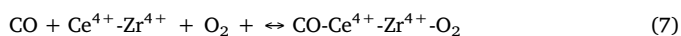
The reaction rate expression is based on the elementary step results:

$$r = k_1 k_2 \frac{P_{CO} P_{O2}}{1 + k_1 P_{CO} + k_1 P_{O2}} \tag{9}$$

The basic assumptions for CO oxidation on all catalysts are as follows:

(1) The chemisorption of CO and O_2 occurs on the Cu-Ce-Zr-O_δ or Ce-Zr-O_δ solid solution to form carbonate species, and then it further decomposes to form CO_2, which is considered the RDS (Eqs. (6) and (8)). (2) The formation of carbonate species on the Cu-Ce-Zr-O_δ or Ce-Zr-O_δ solid solution was evidenced by the in situ DRIFT results.

The modeling expressions (Eqs. (4) and (9)) obtained by the elementary reaction steps of CO oxidation and the power-rate law expressions (see Section 3.5) follow directly from the law of mass action. The direct application of the law of mass action where the orders and the stoichiometric coefficients correspond normally pertains only to the elementary steps of a reaction [41]. Hence, both types of expressions are similar, indicating that CO oxidation over the $CuO/Ce_{0.75}Zr_{0.25}O_{2-\delta}$, $Cu_{0.07}Ce_{0.75}Zr_{0.25}O_{2-\delta}$ and $Ce_{0.75}Zr_{0.25}O_\delta$ catalysts follows two different pathways. It can be seen from the modeling expressions (Eq. (4)) that the order for CO should be between 0 and 1 and that for O_2 is 0, and the modeling expressions (Eq. (9)) indicate that the orders for CO and O_2 should be between 0 and 1, which are validated by the power-rate law expressions from the kinetic results (the exponents for CO are 0.68, 0.8 and 0.75 and those for O_2 are 0.03, 0.07 and 0.12 for $CuO/Ce_{0.75}Zr_{0.25}O_{2-\delta}$, $Cu_{0.07}Ce_{0.75}Zr_{0.25}O_{2-\delta}$ and $Ce_{0.75}Zr_{0.25}O_\delta$, respectively).

Considering the chemisorption and reaction order of CO_2, two supplementary experiments were added in the supporting information.

The first experiment concerns CO_2-TPD over the H_2-pre-reduced CuO/$Ce_{0.75}Zr_{0.25}O_{2-\delta}$ catalyst, and the results suggest that CO_2 can chemisorb on the reduced catalyst (Fig. S4). The second experiment concerns CO_2 chemisorption on the CuO/$Ce_{0.75}Zr_{0.25}O_{2-\delta}$ catalyst under real reaction conditions (0.2 %CO_2 + 0.5%O_2/He balance, 30 mL min^{-1}). It can be seen no signals of CO_2 and CO were monitored under the reaction conditions (Fig. S5). These results verified that Eq. (10) is irreversible and that the oxygen vacancies were mainly refilled by O_2. In addition, the interaction between O_2 and the oxygen vacancies is much stronger than that between CO_2 and the oxygen vacancies in the CO_2/O_2 atmosphere, indicating that almost no chemisorption of CO_2 occurred under real reaction conditions. The irreversible Eq. (2) and the chemisorption of CO and O_2 from different carbonate species that then decompose to yield CO_2 suggest that the order of CO_2 is not involved in the kinetic expressions.

4. Discussion

4.1. Structure-activity relationship and the contribution of active sites

The dispersed CuO species are generally accepted as being the main active sites for the sorption of CO, and CeO_2 is accepted as supplying more oxygen vacancies for oxygen sorption to promote CO oxidation [17,42]. The XRD and TEM results (see Fig. 1 and S2) confirm that CuO crystallites can be removed from CuO/$Ce_{0.75}Zr_{0.25}O_{2-\delta}$ by the nitric acid treatment to produce $Cu_{0.07}Ce_{0.75}Zr_{0.25}O_{2-\delta}$. Further analyses by Raman, XPS and H_2-TPR (see Fig. 2, 4 A and 5) reveal the existence of dispersed CuO species and crystalline CuO on the CuO/$Ce_{0.75}Zr_{0.25}O_{2-\delta}$ surface and confirm that the residual CuO (3.63% from the XRF results) tends to form a Cu-Ce-Zr-O_δ solid solution. Raman spectroscopic analysis shows that the concentration of oxygen vacancies derived from the Cu-Ce-Zr-O_δ solid solution is higher than that from the Ce-Zr-O_δ solid solution (see Fig. 2), which improves the oxygen storage capacity of CuO/$Ce_{0.75}Zr_{0.25}O_{2-\delta}$ and $Cu_{0.07}Ce_{0.75}Zr_{0.25}O_{2-\delta}$. More Ce^{3+} ions are exposed on $Cu_{0.07}Ce_{0.75}Zr_{0.25}O_2$-δ than on the other catalysts, and these ions promote the adsorption and circulation of oxygen (see Fig. 4B and 4C). This phenomenon is also evidenced through O_2-TPD, which shows that the beneficial chemisorption of surface oxygen increases between 300 and 600 °C (see Fig. 6) over $Cu_{0.07}Ce_{0.75}Zr_{0.25}O_{2-\delta}$. The volcano curve also shows that the stronger (lattice oxygen) or weaker (weakly adsorbed oxygen) adsorption intensities of the different reactants slightly hinder the reactions and desorption processes in heterogeneous catalysis [43].

Further investigations show different dispersities of CuO (D) (Table 3) for CuO/$Ce_{0.75}Zr_{0.25}O_{2-\delta}$ (31.3%) and $Cu_{0.07}Ce_{0.75}Zr_{0.25}O_{2-\delta}$ (4.2%). It can be seen from the N_2-BET and H_2-TPR results (Figs. 3 and 5) that the higher accessible surface and larger particle sizes promote the oxygen mobility and reducibility for the catalysts. However, differences in the CuO_x contents caused the hydrogen consumption of CuO/$Ce_{0.75}Zr_{0.25}O_{2-\delta}$ to be higher than that of $Cu_{0.07}Ce_{0.75}Zr_{0.25}O_{2-\delta}$. The TEM and TOF results (see Fig. S2 and Table 3) show that the interface could be the dominant position for CO oxidation, with dispersed CuO species on the more exposed {111} plane of the catalysts. By comparing the catalytic activities of CuO/$Ce_{0.75}Zr_{0.25}O_{2-\delta}$ and $Cu_{0.07}Ce_{0.75}Zr_{0.25}O_{2-\delta}$ (Figs. 7 and 8), it can be determined that highly dispersed CuO species on the surface act as the main active sites in CO oxidation. The Cu^+ derived from either fresh catalyst or the reduction of surface CuO species through transfer electrons is a key active site for adsorbing CO in the reaction mechanism [44]. The high IR band initial areas and IRAQT of the 2103 cm^{-1} band correspond to the Cu^+ carbonyl (Cu^+-CO) in the CO/O_2 co-adsorption process over the CuO/$Ce_{0.75}Zr_{0.25}O_{2-\delta}$ catalyst at temperatures ≤ 100 °C. However, the same band (2103 cm^{-1}) is very low in intensity for the $Cu_{0.07}Ce_{0.75}Zr_{0.25}O_{2-\delta}$ and $Ce_{0.75}Zr_{0.25}O_\delta$ catalysts (as shown in Fig. S3 and Table 6). The Cu^+-CO species is beneficial for CO oxidation because it can substantially lower the activation barrier of CO, which is supported by the activation

energy of CO oxidation over CuO/$Ce_{0.75}Zr_{0.25}O_{2-\delta}$ being much lower than that over the $Cu_{0.07}Ce_{0.75}Zr_{0.25}O_{2-\delta}$ catalyst (see Fig. 9). Thus, the surface CuO species provide the main active sites for CO chemisorption. Jia et al. have also reported that the surface CuO species provide sites for CO chemisorption and that the $Cu_xCe_{1-x}O_{2-\delta}$ solid solution promotes the activation of oxygen species over the CuO/$Ce_{1-x}Cu_xO_{2-\delta}$ catalyst [17].

The other active sites in CO oxidation are the solid solutions. Compared with the Ce-Zr-O_δ solid solution in the $Ce_{0.75}Zr_{0.25}O_\delta$ catalyst, the formation of a Cu-Ce-Zr-O_δ solid solution in CuO/$Ce_{0.75}Zr_{0.25}O_{2-\delta}$ and $Cu_{0.07}Ce_{0.75}Zr_{0.25}O_{2-\delta}$ provides higher oxygen vacancy concentrations and better redox properties, as shown by the Raman, H_2-TPR and O_2-TPD results. Note that the H_2-TPR results indicate a greater amount of exposed Ce^{3+} (and Ce^{4+}) on the higher accessible surface areas over the $Cu_{0.07}Ce_{0.75}Zr_{0.25}O_2$-δ catalyst, and these ions have a synergistic effect with the CuO species to promote the reduction of CuO_x species and to result in the very limited number of exposed surface Ce species. Shan et al. obtained a similar conclusion in which the formation of a $Cu_xCe_{1-x}O_{2-\delta}$ solid solution could improve the redox properties of Ce^{4+}/Ce^{3+} and promote the reactions [45]. Therefore, the Cu-Ce-Zr-O_δ solid solution not only promotes the redox properties of the catalysts but also accelerates the activation of oxygen species in CuO/$Ce_{0.75}Zr_{0.25}O_{2-\delta}$ and $Cu_{0.07}Ce_{0.75}Zr_{0.25}O_{2-\delta}$. The carbonate species formed by the reaction of adsorbing CO with surface oxygen (1505 + 1058, 1342, 1633 and 1303 cm^{-1}) were observed in the CO/O_2 reaction process on all the catalysts, suggesting that Cu species interact with Ce species to provide secondary active sites to adsorb CO and O_2 [21]. Furthermore, both the IR band initial areas and IRAQT of the carbonate peaks generated from the Cu-Ce-Zr-O_δ solid solution are higher than those of the Ce-Zr-O_δ solid solution in the $Ce_{0.75}Zr_{0.25}O_\delta$ catalyst at ≥ 100 °C. Hence, the two other active sites for CO and O_2 adsorption could also produce CO oxidation. In conclusion, after combining the normalized rates for CO oxidation of the CuO/$Ce_{0.75}Zr_{0.25}O_{2-\delta}$, $Cu_{0.07}Ce_{0.75}Zr_{0.25}O_{2-\delta}$ and $Ce_{0.75}Zr_{0.25}O_\delta$ catalysts (Figs. 7 and 8), the contribution of different active sites in CO oxidation decreases in the order of surface CuO_x species > Cu-Ce-Zr-O_δ solid solution > Ce-Zr-O_δ solid solution.

4.2. CO oxidation mechanism over the CuO/$Ce_{0.75}Zr_{0.25}O_{2-\delta}$, $Cu_{0.07}Ce_{0.75}Zr_{0.25}O_{2-\delta}$ and $Ce_{0.75}Zr_{0.25}O_\delta$ catalysts

The IR band initial areas of the peak corresponding to the adsorption of CO onto Cu^+ (2103 cm^{-1}) over the catalysts were observed (Table 6). The CO molecule forms strong bonds with metal cations depending on the back donation of electrons from the surface cations into the antibonding π-orbital, which are generally supplied by the d-orbital of the metal [45]. The outer shell electron distributions of Cu^+, Ce^{3+} and Ce^{4+} correspond to $3d^{10}$, $4f^1$, and a grouping of $5s^2$, $4d^{10}$ and $5p^6$, respectively. The d-orbital of Cu^+ is completely or nearly full of electrons; thus, compared with Ce^{3+} and Ce^{4+}, Cu^+ tends to establish stronger bonding with CO [46]. Therefore, the CO preferentially adsorbs onto the Cu^+ on all catalysts, which is in agreement with the results of our previous investigation [18].

The kinetics of the CuO/$Ce_{0.75}Zr_{0.25}O_{2-\delta}$, $Cu_{0.07}Ce_{0.75}Zr_{0.25}O_{2-\delta}$ and $Ce_{0.75}Zr_{0.25}O_\delta$ catalysts were investigated in this work. The partial pressure of CO strongly influences the CO conversion for all the catalysts, whereas the partial pressure of O_2 gradually affects the CO conversion in the order of CuO/$Ce_{0.75}Zr_{0.25}O_{2-\delta}$, $Cu_{0.07}Ce_{0.75}Zr_{0.25}O_{2-\delta}$ and $Ce_{0.75}Zr_{0.25}O_\delta$. The rate expressions exponents are 0.68, 0.8 and 0.75 for CO and 0.03, 0.07 and 0.12 for O_2 corresponding to CuO/$Ce_{0.75}Zr_{0.25}O_{2-\delta}$, $Cu_{0.07}Ce_{0.75}Zr_{0.25}O_{2-\delta}$ and $Ce_{0.75}Zr_{0.25}O_\delta$. These results indicate that the reaction is mainly dependent on the adsorption of CO for all the catalysts and that lattice oxygen is more important than gas-phase O_2 in CO oxidation on CuO/$Ce_{0.75}Zr_{0.25}O_{2-\delta}$; the results also indicate that large amounts of gas-phase O_2 may participate in the reaction on $Cu_{0.07}Ce_{0.75}Zr_{0.25}O_{2-\delta}$ and $Ce_{0.75}Zr_{0.25}O_\delta$, which is consistent
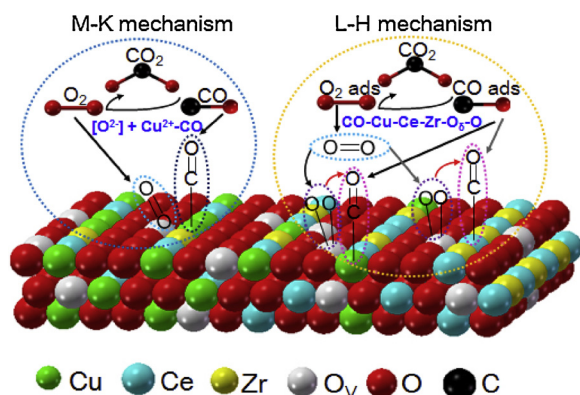
Scheme 1. Reaction mechanism model of CO oxidation over the CuO/Ce$_{0.75}$Zr$_{0.25}$O$_{2-\delta}$, Cu$_{0.07}$Ce$_{0.75}$Zr$_{0.25}$O$_{2-\delta}$ and Ce$_{0.75}$Zr$_{0.25}$O$_\delta$ catalysts.

with the in situ DRIFT results (see Fig. 10). Sedmak et al. reported that the exponents of the reactants in the CO preferential oxidation are 1 for CO and 0.15 $\pm$ 0.025 for O$_2$ via Liu and Flytazani-Stephanopoulus's kinetic model [15,19]. The Arrhenius plots show apparent activation energies of 53 $\pm$ 3 kJ/mol for CuO/Ce$_{0.75}$Zr$_{0.25}$O$_{2-\delta}$, 105 $\pm$ 5 for Cu$_{0.07}$Ce$_{0.75}$Zr$_{0.25}$O$_{2-\delta}$ and 115 $\pm$ 6 kJ/mol for Ce$_{0.75}$Zr$_{0.25}$O$_\delta$, implying that CuO species on the catalyst surface could greatly reduce the activation energy for CO adsorption.

The normalized reaction rates by accessible surface area are 0.14 $\times$ 10^{-8} (90 °C), 0.098 $\times$ 10^{-8} (130 °C), and 0.096 $\times$ 10^{-8} (190 °C) mol·m^{-2}·s^{-1} for the CuO/Ce$_{0.75}$Zr$_{0.25}$O$_{2-\delta}$, Cu$_{0.07}$Ce$_{0.75}$Zr$_{0.25}$O$_{2-\delta}$ and Ce$_{0.75}$Zr$_{0.25}$O$_\delta$ catalysts, respectively. The CuO/Ce$_{0.75}$Zr$_{0.25}$O$_{2-\delta}$ catalyst has a higher normalized reaction rate per unit of surface area and time at lower temperature regions than that of the Cu$_{0.07}$Ce$_{0.75}$Zr$_{0.25}$O$_{2-\delta}$ and Ce$_{0.75}$Zr$_{0.25}$O$_\delta$ catalysts due to the large amount of surface active CuO$_x$ species on the CuO/Ce$_{0.75}$Zr$_{0.25}$O$_{2-\delta}$ catalyst. The in situ DRIFT and kinetics results reveal two types of CO species on the three different active sites: most of the adsorbed CO is on the surface of Cu$^+$ (2103 cm^{-1}) and is chemically bonded to surface oxygen to form different carbonate species on the Cu-Ce-Zr-O$_\delta$ and Ce-Zr-O$_\delta$ solid solutions, confirming that the CO adsorption is the RDS for CO oxidation. However, the IR band initial areas of the carbonate peaks for Cu$_{0.07}$Ce$_{0.75}$Zr$_{0.25}$O$_{2-\delta}$ are stronger than those for CuO/Ce$_{0.75}$Zr$_{0.25}$O$_{2-\delta}$ because more Ce^{3+} exposed after the nitric acid treatment promotes O$_2$ chemisorption and possesses a higher surface area to chemisorb CO/O$_2$ on the Cu-Ce-Zr-O$_\delta$ solid solution, thus forming more carbonate species on the surface of Cu$_{0.07}$Ce$_{0.75}$Zr$_{0.25}$O$_{2-\delta}$. Hence the L-H mechanism is more important than the M-K mechanism over the Cu$_{0.07}$Ce$_{0.75}$Zr$_{0.25}$O$_{2-\delta}$ and Ce$_{0.75}$Zr$_{0.25}$O$_\delta$ catalysts because of the absence of surface-dispersed CuO$_x$ species. The two different mechanisms should occur over all catalysts. According to the M-K mechanism, the CO first adsorbs onto the active sites of the catalyst surface and reacts with lattice oxygen to form gas-phase CO$_2$, leaving oxygen vacancies that can reform into lattice oxygen via O$_2$ to complete the cycle (see Scheme 1). Meanwhile, the L-H mechanism also involves the reactions of the adsorbed CO and adsorbed oxygen on the Cu-Ce-Zr-O$_\delta$ solid solution or the Ce-Zr-O$_\delta$ solid solution in the catalysts to form carbonate species, followed by generation of CO$_2$, which desorbs into the gas phases (see Scheme 1). The detailed reaction pathways, including transformed reactive species, can be seen in Fig. S6. The M-K mechanism becomes more important than the L-H mechanism over the CuO/Ce$_{0.75}$Zr$_{0.25}$O$_{2-\delta}$ catalyst. The L-H mechanism is more important than the M-K mechanism over the Cu$_{0.07}$Ce$_{0.75}$Zr$_{0.25}$O$_{2-\delta}$ and Ce$_{0.75}$Zr$_{0.25}$O$_\delta$ catalysts because of the absence of surface-dispersed CuO$_x$ species.

5. Conclusions

In this study, the relationship between the structural properties and catalytic behaviors of the CuO/Ce$_{0.75}$Zr$_{0.25}$O$_{2-\delta}$, Cu$_{0.07}$Ce$_{0.75}$Zr$_{0.25}$O$_{2-\delta}$ and Ce$_{0.75}$Zr$_{0.25}$O$_\delta$ catalysts was investigated. CuO/Ce$_{0.75}$Zr$_{0.25}$O$_{2-\delta}$ contains surface-dispersed CuO species and a Cu-Ce-Zr-O$_\delta$ solid solution as the active sites. The surface-dispersed CuO species are removed via a nitric acid treatment to produce Cu$_{0.07}$Ce$_{0.75}$Zr$_{0.25}$O$_{2-\delta}$. The results show that the catalytic activity for CO oxidation decreases in the order of CuO/Ce$_{0.75}$Zr$_{0.25}$O$_{2-\delta}$ > Cu$_{0.07}$Ce$_{0.75}$Zr$_{0.25}$O$_{2-\delta}$ > Ce$_{0.75}$Zr$_{0.25}$O$_\delta$.

Because of the reaction sensitivity, CO prefers linear chemisorption in the following order: on surface CuO$_x$ species > carbonate species on a Cu-Ce-Zr-O$_\delta$ solid solution > carbonate species on a Ce-Zr-O$_\delta$ solid solution. Further investigation via kinetics studies and in situ DRIFT showed that CO adsorption is the RDS for CO oxidation. Additionally, the M-K mechanism is likely a critical reaction pathway for the interfacial reaction of CO and the CuO/Ce$_{0.75}$Zr$_{0.25}$O$_{2-\delta}$ catalyst, although the L-H mechanism cannot be ignored. The L-H mechanism is likely the major mechanism over the Cu$_{0.07}$Ce$_{0.75}$Zr$_{0.25}$O$_{2-\delta}$ and Ce$_{0.75}$Zr$_{0.25}$O$_\delta$ catalysts, whereas the contribution of the M-K mechanism is minor. Although Cu-Ce-Zr-O$_\delta$ can adsorb CO, the more important role of Cu-Ce-Zr-O$_\delta$ is to improve O$_2$ adsorption, thus promoting the oxygen reaction cycle.

Appendix A. Supplementary data

Supplementary material related to this article can be found, in the online version, at doi:https://doi.org/10.1016/j.apcata.2018.07.026.

References

[1] N. Almana, S.P. Phivilay, P. Laveille, M.N. Hedhili, P. Fornasiero, K. Takanabe, J.M. Basset, J. Catal. 340 (2016) 368–375.
[2] B. Schönbrod, F. Mariño, G. Baronetti, M. Laborde, Int. J. Hydrogen Energy 34 (2009) 4021–4028.
[3] N. Li, Q.Y. Chen, L.F. Luo, W.X. Huang, M.F. Luo, G.S. Hua, J.Q. Lu, Appl. Catal. B: Environ. 142–143 (2013) 523–532.
[4] H.H. Liu, Y. Wang, A.P. Jia, S.Y. Wang, M.F. Luo, J.Q. Lu, Appl. Surf. Sci. 314 (2014) 725–734.
[5] O.H. Laguna, A. Pérez, M.A. Centeno, J.A. Odriozola, Appl. Catal. B: Environ. 176–177 (2015) 385–395.
[6] H. He, H.X. Dai, K.W. Wong, C.T. Au, Appl. Catal. A Gen. 251 (2003) 61–74.
[7] R.D. Zhang, W.Y. Teoh, R. Amal, B.H. Chen, S. Kaliaguine, J. Catal. 272 (2010) 210–219.
[8] J.L. Ayastuy, A. Gurbani, M.P. Gonza´lez-Marcos, M.A. Gutiérrez-Ortiz, Int. J. Hydrogen Energy 37 (2012) 1993–2006.
[9] X.F. Dong, H.B. Zou, W.M. Lin, Int. J. Hydrogen Energy 31 (2006) 2337–2344.
[10] L.J. Liu, Z.J. Yao, B. Liu, L. Dong, J. Catal. 275 (2010) 45–60.
[11] L. Qi, Q. Yu, Y. Dai, C.J. Tang, L.J. Liu, H.L. Zhang, F. Gao, L. Donga, Y. Chen, Appl. Catal. B: Environ. 119–120 (2012) 308–320.
[12] G.M. Javier, B.L. Agustín, G.G. Avelina, Appl. Catal. B: Environ. 152–153 (2014) 99–107.
[13] M.F. Luo, J.M. Ma, J.Q. Lu, Y.P. Song, Y.J. Wang, J. Catal. 246 (2007) 52–59.
[14] H. Yoshida, N. Yamashita, S. Ijichi, Y. Okabe, S. Misumi, S. Hinokuma, M. Machida, ACS Catal. 5 (2015) 6738–6747.
[15] G. Sedmak, S. Hočevar, J. Levec, J. Catal. 213 (2003) 135–150.
[16] G. Sedmak, S. Hočevar, J. Levec, J. Catal. 222 (2004) 87–99.
[17] A.P. Jia, G.S. Hu, L. Meng, Y.L. Xie, J.Q. Lu, M.F. Luo, J. Catal. 289 (2012) 199–209.
[18] F. Bin, X.L. Wei, B. Li, S.H. Kwan, Appl. Catal. B: Environ. 162 (2015) 282–288.
[19] W. Liu, M. Flytzani-Stephanopoulos, J. Catal. 153 (1995) 304–317.
[20] F.C. Lee, Y.F. Lu, F.C. Chou, C.F. Cheng, R.M. Ho, D.H. Tsai, J. Phys. Chem. C 120 (2016) 13638–13648.
[21] Y.N. Zheng, K.Z. Li, H. Wang, H. Wang, D. Tian, Y.G. Wei, X. Zhu, C.H. Zeng, Y.M. Luo, J. Catal. 344 (2016) 365–377.
[22] R.Z. Zhao, Q.L. Hao, F. Bin, R.N. Kang, B.J. Dou, Combust. Sci. Technol. 189 (2017) 1394–1415.
[23] F. Bin, X.L. Wei, T. Li, D.L. Liu, Q.L. Hao, B.J. Dou, Proc. Combust. Inst. 36 (2017) 4193–4200.
[24] Z.Y. Pu, X.S. Liu, A.P. Jia, Y.L. Xie, J.Q. Lu, M.F. Luo, J. Phys. Chem. C 112 (2008) 15045–15051.

[25] J.R. Jensen, T. Johannessen, H. Livbjerg, Appl. Catal. A Gen. 266 (2004) 117–122.

[26] M. Shacham, M.B. Cutlip, M. Elly, Copyright, Polymath (2006), http://www.polymath-software.com.

[27] Z.Q. Yang, D.S. Mao, X.M. Guo, G.Z. Lu, J. Rare Earth 32 (2014) 117–123.

[28] J.R. McBride, K.C. Hass, B.D. Poindexter, W.H. Weber, J. Appl. Phys. 76 (1994) 2435–2441.

[29] S. Velu, K. Suzuki, T. Osaki, Catal. Lett. 62 (1999) 159–167.

[30] C. He, Y.K. Yu, L. Yue, N.L. Qiao, J.J. Li, Q. Shen, W.J. Yu, J.S. Chen, Z.P. Hao, Appl. Catal. B: Environ. 147 (2014) 156–166.

[31] J.J. Shi, Y.Y. Wang, W.C. Du, Z.Y. Hou, Carbon 99 (2016) 330–337.

[32] D.F. Jin, J. Gao, Z.Y. Hou, G. Yan, X.Y. Lu, Y.G. Zhu, X.M. Zheng, Appl. Catal. A Gen. 352 (2009) 259–264.

[33] L. Katta, P. Sudarsanam, G. Thrimurthulu, B.M. Reddy, Appl. Catal. B: Environ. 101 (2010) 101–108.

[34] X.M. Liao, W. Chu, X.Y. Dai, V. Pitchon, Appl. Catal. A Gen. 449 (2012) 131–138.

[35] X.L. Guo, J. Li, R.X. Zhou, Fuel 163 (2016) 56–64.

[36] S.H. Zeng, Y. Wang, S.P. Ding, J.J.H.B. Sattler, E. Borodina, L. Zhang,

B.M. Weckhuysen, H.Q. Su, J. Power Sources 256 (2014) 301–311.

[37] A.P. Jia, S.Y. Jiang, J.Q. Lu, M.F. Luo, J. Phys. Chem. C 114 (2010) 21605–21610.

[38] T. Caputo, L. Lisi, R. Pirone, G. Russo, Appl. Catal. A Gen. 348 (2008) 42–53.

[39] I. Atribak, A. Bueno-López, A. García-García, J. Catal. 259 (2008) 123–132.

[40] H.S. Fogler, Elements of Chemical Reaction Engineering, 4 th edition, (2006), p. 839.

[41] J.B. Butt, Reaction Kinetics and Reactor Design, Prentice-Hall, Englewood Cliffs, New Jersey, 1980, pp. 6–7.

[42] M. Moreno, L. Bergamini, G.T. Baronetti, M.A. Laborde, F.J. Mariňo, Int. J. Hydrogen Energy 35 (2010) 5918–5924.

[43] Y. Mao, J.F. Chen, H.F. Wang, P. Hu, Chin. J. Catal. 36 (2015) 1596–1605.

[44] A. Martínez-Arias, A.B. Hungría, M. Fernández-García, J.C. Conesa, G. Munuera, J. Phys. Chem. B 108 (2004) 17983–17991.

[45] W. Shan, W. Shen, C. Li, Chem. Mater. 15 (2003) 4761–4767.

[46] A. Hornés, P. Bera, A.L. Cámara, D. Gamarra, G. Munuera, A.M. Arias, J. Catal. 268 (2009) 367–375.